ORNL/SPR-2016/329

FY 2016 Status Report: CIRFT Testing on Spent Nuclear Fuels and Hydride Reorientation Study

Fuel Cycle Research & Development

Prepared for
US Department of Energy
Used Fuel Disposition Campaign

J.-A. Wang, H. Wang, Yong Yan
B. B. Bevard, J. M. Scaglione
Oak Ridge National Laboratory

August 4, 2016
M4FT-16OR080202033

ORNL/SPR-2016/329

Materials Science and Technology Division

FY 2016 Status Report: CIRFT Testing on Spent Nuclear Fuels and Hydride Reorientation Study

Jy-An John Wang, Hong Wang, and Yong Yan

Program Managers
Bruce Bevard and John Scaglione

Date Published: August 4, 2016

Prepared by
OAK RIDGE NATIONAL LABORATORY
Oak Ridge, TN 37831-6283
managed by
UT-BATTELLE, LLC
for the
US DEPARTMENT OF ENERGY
under contract DE-AC05-00OR22725

This page intentionally left blank.

SUMMARY

This report provides a detailed description of the Cyclic Integrated Reversible-Bending Fatigue Tester (CIRFT) testing conducted on spent nuclear fuel (SNF) rods in FY 2016, including hydride reorientation test results.

Contact-based measurement, or three-LVDT-based curvature measurement, of SNF rods has proven to be quite reliable in CIRFT testing. However, how the linear variable differential transformer (LVDT) head contacts the SNF rod may have a significant effect on the curvature measurement, depending on the magnitude and direction of rod curvature. To correct such contact/curvature issues, sensor spacing, defined as the amount of separation between the three LVDT probes, is a critical measurement that can be used to calculate rod curvature once the deflections are obtained.

Sensor spacing correction can be determined by using chisel-type probes. However, after careful examination this year, the method proved to be difficult to implement in a hot cell environment and thus could not be implemented effectively. A correction based on the proposed equivalent gauge length has the flexibility and accuracy required for this study and hence was used as an appropriate correction factor.

These recently developed CIRFT data analyses procedures were also integrated into FY 2016 CIRFT testing results for the curvature measurements.

The variations in fatigue life are provided in terms of moment, equivalent stress, curvature, and equivalent strain for the tested SNFs. The equivalent stress plot collapsed the data points from all of the SNFs into a single zone. A detailed examination revealed that, at same stress level, fatigue lives display a descending order as follows: H. B. Robinson Nuclear Power Station (HBR), Limerick Nuclear Power Station (LMK), mixed uranium-plutonium oxide (MOX). If looking at the strain, then LMK fuel has a slightly longer fatigue life than HBR fuel, but the difference is subtle.

The knee point of endurance limit in the curve of moment and curvature or equivalent quantities is more clearly defined for LMK and HBR fuels.

The treatment affects the fatigue life of specimens. Both a drop of 12 in. and radial hydride treatment (RHT) have a negative impact on fatigue life. The effect of thermal annealing on MOX fuel rods was relatively small at higher amplitude but became significant at low amplitude of moment. Thermal annealing tended to extend the fatigue life of MOX fuel rod specimens. However, for HR4 testing, the thermal annealing treatment showed a negative impact on the fatigue life of the HBR rod.

ACKNOWLEDGMENTS

This research was jointly sponsored by the Office of Nuclear Research of U.S. Nuclear Regulatory Commission (NRC) and the US Department of Energy (DOE) Used Fuel Disposition Campaign (UFDC) under DOE contract DE-AC05-00OR22725 with UT-Battelle, LLC. The authors thank NRC program manager Michelle Bales and ORNL program managers Bruce Bevard and John Scaglione for their support and guidance during the project, Chuck Baldwin for post-irradiation examination (PIE), Josh Schmidlin for fuel rod cutting and dimension measurement, Bryan Woody and Scott Thurman for hot-cell operation support, Brian Sparks and Randy Parten for drawing and machining support, and Lianshan Lin for reviewing the report.

This page intentionally left blank.

CONTENTS

LIST OF FIGURES

This page intentionally left blank.

LIST OF TABLES

This page intentionally left blank.

ACRONYMS

AP	alumina pellets
BWR	boiling water reactor
CIRFT	Cyclic Integrated Reversible-Bending Fatigue Tester
DOE	US Department of Energy
FCRD	Fuel Cycle Research & Development
FEA	finite-element analysis
FY	fiscal year
GWd/MTU	gigawatt-days per metric ton of uranium
HBR	H. B. Robinson Nuclear Power Station
HBU	high burnup
ID	identification numbers
LMK	Limerick Nuclear Power Station
LVDT	linear variable differential transformer
MOX	mixed uranium-plutonium oxide
NA	North Anna Power Station
NCT	normal conditions of transport
NRC	US Nuclear Regulatory Commission
NUREG	Nuclear Regulatory Commission technical report
NUREG/CR	NUREG contractor report
OD	outer diameter
ORNL	Oak Ridge National Laboratory
PCI	peripheral component interconnect
PIE	post-irradiation examination
PNNL	Pacific Northwest National Laboratory
PPI	pellet-to-pellet interface
PWR	pressurized water reactor
RT	room temperature
SNF	spent nuclear fuel
SS	stainless steel
SSAP	stainless steel alumina pellets
UFDC	Used Fuel Disposition Campaign
SNF	spent nuclear fuel

This page intentionally left blank.

USED FUEL DISPOSITION CAMPAIGN

FY 2016 Status Report: CIRFT Testing on Spent Nuclear Fuels and Hydride Reorientation Study

1. CYCLIC INTEGRATED REVERSIBLE-BENDING FATIGUE TESTER

The Cyclic Integrated Reversible-Bending Fatigue Tester (CIRFT), developed by ORNL,[1,2,3,4,5,6,7,8] consists of a U-frame that includes two rigid arms, connecting plates, and universal testing machine links, as shown in Fig. 1. The rod specimen is coupled to the rigid arms through two specially designed grips. The U-frame setup is oriented in a horizontal plane and is driven by electromagnetic force–based Bose dual linear motors. With help from the coupling, linear motions applied at the loading points of the rigid arms are converted into bending moments. The dual linear motor (model LM2) test bench has a maximum load capacity of ±3,000 N and a maximum stroke of ±25.6 mm. Bending is imposed through a U-frame with dual driving points and a 101.60 mm loading arm. Under a pair of forces or displacements that face outward, the rigid arms are opened, and bending moments force the rod to deflect outward (away from operator). Under a pair of forces facing each other, the rigid arms are closed, forcing the rod to deflect inward. The CIRFT can deliver dynamic loading to a rod specimen in the load-control mode at 5 to 10 Hz. The current configuration enables the system to test a rod 9.70 mm to 11.74 mm in diameter, 152.40 mm (6 in.) in length, and 50.80 mm (2 in.) in gage section. Three LVDTs measure rod deflections at three adjacent points within the gage section to determine rod curvature, which is then correlated to the applied moment to characterize the mechanical property of the bending rod. Online monitoring can capture mechanical property changes to reveal fatigue behavior during testing.

These recently developed CIRFT data analyses procedures, as outlined in Section 1.3.3, were also integrated into FY 2016 CIRFT testing results for the curvature measurements.

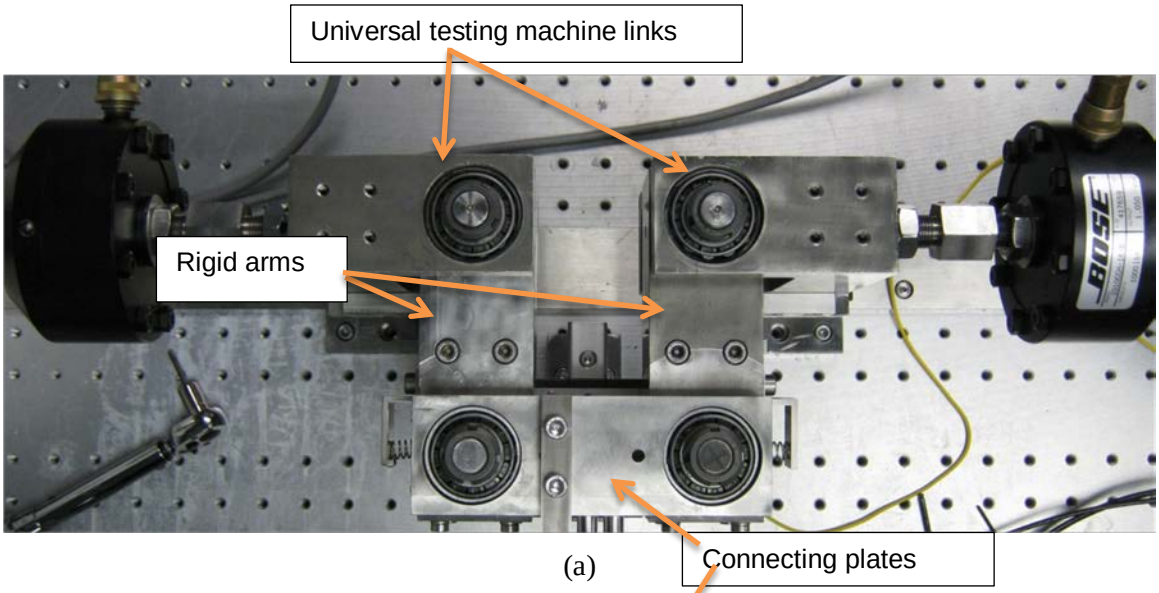
Universal testing machine links
Rigid arms
Connecting plates

(a)

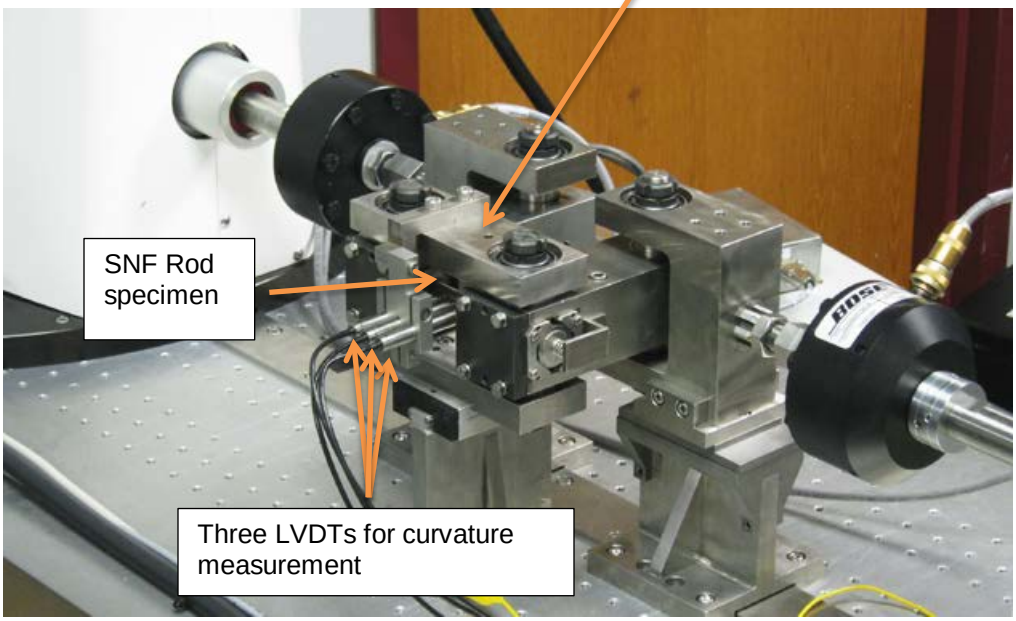
SNF Rod specimen
Three LVDTs for curvature measurement

(b)

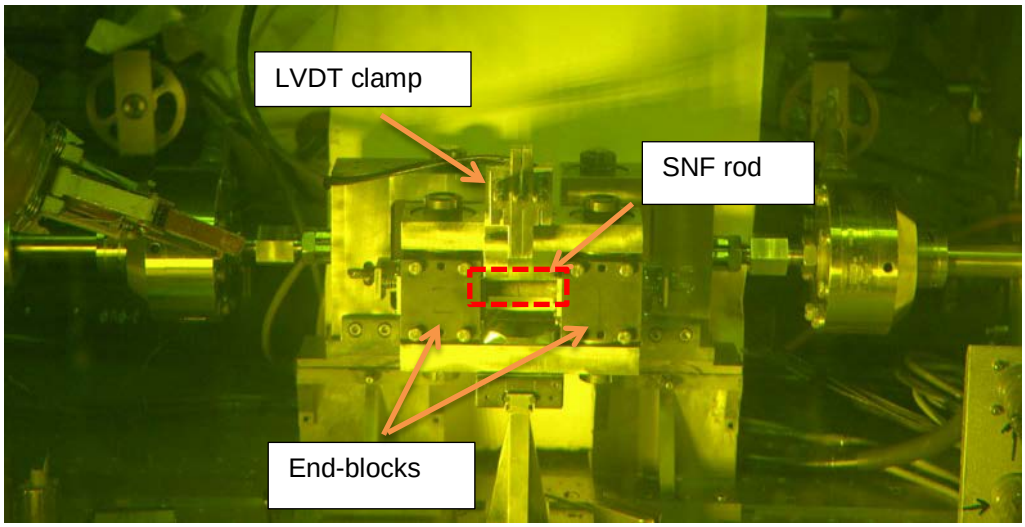

(c)

Fig. 1. (a) Horizontal layout of ORNL U-frame setup, (b) rod specimen under test and three LVDTs for curvature measurement (operator is facing the three LVDTs), and (c) front view of CIRFT installed in ORNL hot cell.

1.1 Moment and Curvature Calculations

Measurement data are converted into the applied moment and curvature based on the load channel (load1 and load2) information, the loading arm length (101.60 mm), and LVDT data (LVDT1, 2, and 3).

The moment was estimated by

$$M = F \times L \,, \tag{1}$$

where F is the averaged value of applied loads (load1 and load2) from the Bose dual motors, and L is the loading arm length, 101.60 mm.

Theoretically, the bending radius and maximum strain of a rod can be estimated on the basis of the traveling displacement at the loading points of the rigid arm. However, the displacement measured includes the contribution of the compliant layers, protective epoxy layer between rigid sleeve and SNF rod, which depends on the materials used in the compliant layers and the level of loading.

To address this issue, direct measurement of the specimen displacement at three adjacent points along the rod method was adopted[9] and has been implemented to evaluate the curvature of a bending rod in this study.[2,3]

Given any curve C and a point P on it, there is a unique circle or line which most closely approximates the curve near P, the osculating circle at P. The curvature of C at P is then defined to be the curvature of that circle or line. The radius of curvature is defined as the reciprocal of the curvature. Given the deflections from three LVDTs, d_1, d_2, and d_3, as shown in Fig. 2, the curvature κ of the bending rod can be evaluated as follows:

$$\kappa = [(x_0 - d_2)^2 + y_0^2]^{-1/2}, \tag{2}$$

$$x_0 = \frac{-2m_a m_b h - m_a(d_2 + d_3) + m_b(d_1 + d_2)}{2(m_b - m_a)},$$

$$y_0 = -\frac{1}{m_a}\left(x_0 - \frac{d_1 + d_2}{2}\right) - \frac{h}{2},$$

where

$$m_a = \frac{h}{d_2 - d_1},$$

$$m_b = \frac{h}{d_3 - d_2},$$

and h is the sensor distance, 12 mm.

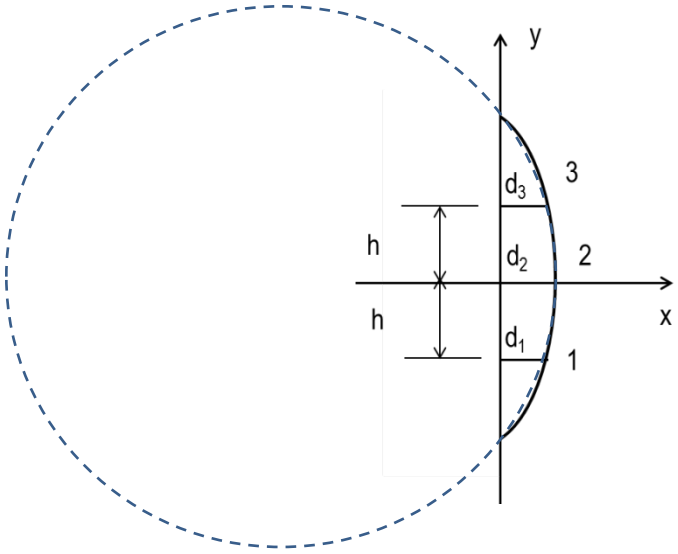

Fig. 2. Determination of the bending curvature of the rod by use of deflections measured at three points.

The arrangement of the three LVDTs and their installation in the setup can be seen in Fig. 3. An equivalent strain-stress curve (illustrated in Eq. 3) can be obtained under the assumption that the SNF rod can be idealized as a linear elastic homogeneous material without considering the effects induced by pellet-clad interaction. The equivalent stress was calculated using

$$\sigma = M \times y_{max}/I\ , \qquad (3)$$

where I is the moment of inertia of the SNF system, $I = I_c + I_p$, I_c and I_p are moments of inertia of cladding and pellet, respectively, and y_{max} is the maximum distance to the neutral axis of the test rod of the section and is measured by the radius of the cladding. The calculation of stress disregards the difference in elastic moduli between the cladding and pellets.

The equivalent strain is then

$$\varepsilon = \kappa \times y_{max}\,. \qquad (4)$$

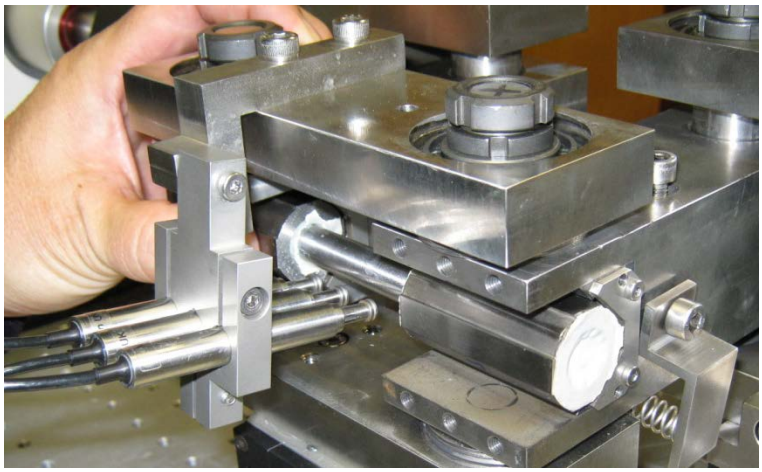

Fig. 3. Grip design of CIRFT with one end-block removed.

1.2 Sensor Spacing Correction for Curvature Measurement

The contact of the LVDT probe with the rod under testing depends on the bending direction and induced curvature, especially when the contact is a disk with a flat head. This resulted in the deviation of sensor spacing from the ideal condition (Fig. 4, with $\kappa=0$).

For positive curvature when tensile load is applied to the U-frame, actual sensor spacing h_2 is

$$h_2 = h + \Delta h, \tag{5}$$

and for negative curvature when compressive load is applied to the U-frame, actual sensor spacing h_1 is

$$h_1 = h - \Delta h. \tag{6}$$

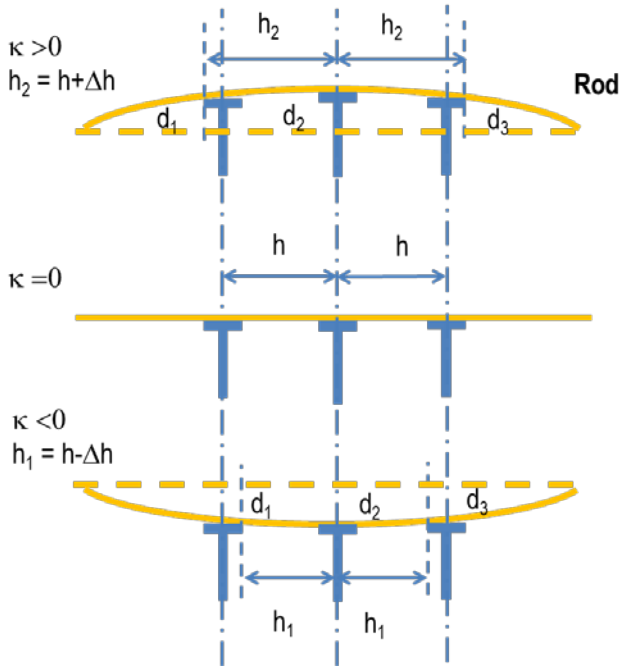

Fig. 4. Deflections measured by LVDTs may be at different points from initial positions, and sensor spacing h needs to be corrected.

A polycarbonate rod (0.4375 in. diameter and 6 in. length) specimen PC01 was tested under -6 mm and +6 mm with disk-head LVDTs. Curvatures in the positive and negative directions appeared to be quite different, as shown in Fig. 5.

The same specimen PC01 was tested under the same level of applied displacement, but curvatures were based on chisel head LVDTs. The curvatures in both directions were very close near 2 m^{-1}. The repeatable results indicated that the PC01 behaved elastically as designed, and at the same time, the effect of chisel head on the curvature measurement was negligible.

Analysis revealed the following:

- For a positive curvature induced by tension on the U-frame, a sensor adjustment of 2.90 mm is needed to have the disk-based measurement match with the chisel-based measurement.

- For a negative curvature induced by compression on the U-frame, a sensor adjustment of 2.40 mm is needed to have the disk-based measurement match with the chisel-based measurement.

The sensor spacing adjustments obtained for the two conditions will be used in the data analysis in Sect. 2.

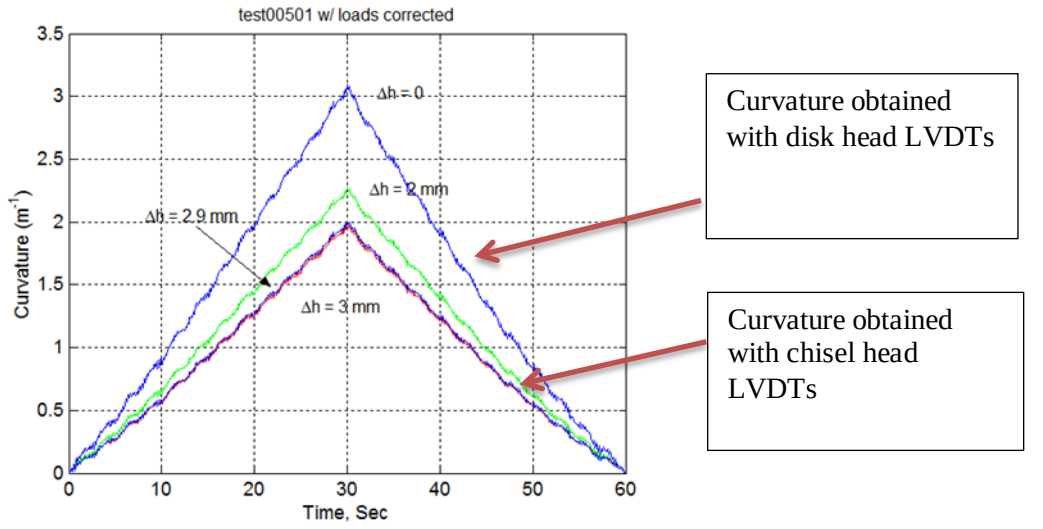

(a)

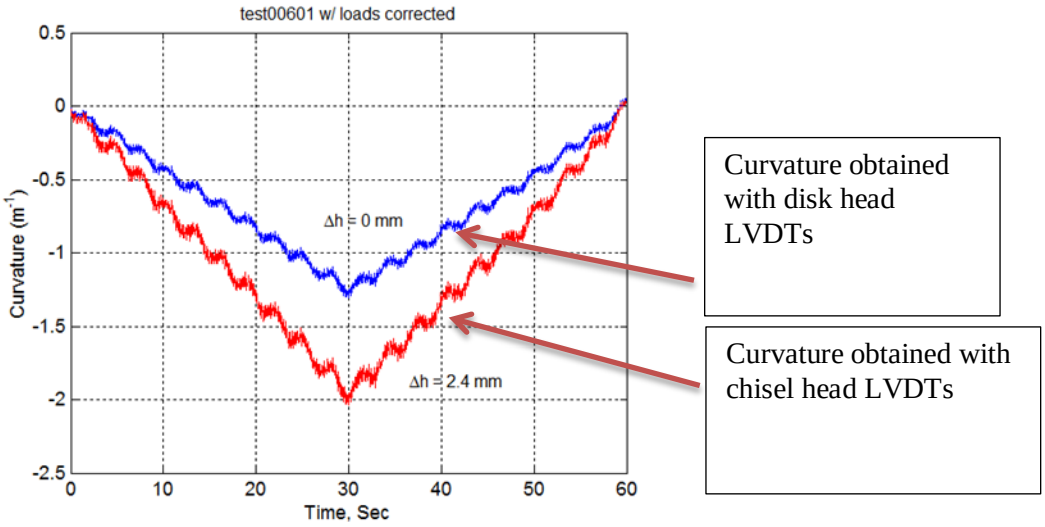

(b)

Fig. 5. (a) For a positive curvature induced by tension on the U-frame, a sensor adjustment of 2.9 mm is needed to have the disk-based measurement match with the chisel-based measurement. (b) For the negative curvature induced by compression on the U-frame, a sensor adjustment of 2.4 mm is needed to have the disk-based measurement match with the chisel-based measurement.

1.3 Verification of Curvature Measurement

1.3.1 Technical Issues

Technical issues exist regarding the curvature measurement in CIRFT testing.

1) Can the curvature measured by the three LVDTs be evaluated? If so, how?
2) How close is the corrected curvature to the actual curvature?
3) Is the correction method applicable to all the levels of curvature?
4) Is the correction method applicable to both static and dynamic cases?

1.3.2 Technical Approach

ORNL proposed to use strain gage measurements to further benchmark the three LVDT curvature measurements. The rationale behind this is as follows:

1) When using a homogenous bending rod, the maximum strain at the extreme fiber can be evaluated because the estimate of that strain has been established theoretically. The deformation of the rod shall be limited within the elastic region of the material to enable the calculation to be effective.
2) The three-LVDT-based curvatures in step 1 can be converted into the strain at the extreme fiber.
3) The strain at the extreme fiber can be measured by a strain gage.
4) The strain-gage-based strain in step 3 can thus be compared with the three-LVDT-based strains to verify the curvature measurement in step 1.

1.3.3 Base Consideration in Data Analyses

The following aspects were considered:

1) The LVDT-based strain calculation was based on the discussion in Section 1.1.
2) The correction was based on the assumption that the gage lengths in both the peak and valley of one data block were equal. The half gage length Lg/2 was calculated according to the following equation.

$$Lg/2 = \sqrt{2d_2/\kappa}, \quad (7)$$

where d_2 is the middle LVDT reading in m and κ is the calculated curvature in m^{-1}.

3) The gage-based strain was obtained according the following equation.

$$\varepsilon = 10^6/(0.25*V_{BR}*A*S_g), \quad (8)$$

where ε is micro strain or με, V_{BR} is the bridge voltage, A is the amplification, and S_g is the gage factor.

4) The strain can be estimated according to the given condition of the rod by

$$\varepsilon = (M/EI)y_{max}, \quad (9)$$

where M is the applied moment amplitude, EI is the flexural rigidity, and y_{max} is the same as previously defined. For example, EI = 42.8 Nm^2 and y_{max} = 4.78mm for a SS304 surrogate rod.

1.3.4 Experimental Results

ORNL accomplished the following.

1) Purchased a four-channel strain gage signal conditioning amplifier Micro Measurement 2310B.

2) Integrated the conditioning amplifier 2310B into the PCI-82 control box in Bose testing machine (L218, 4515).

3) Studied the strain gages for the surrogate rod in-out cell testing in both small and large deformation cases.

4) Performed the CIRFT test on the surrogate rod made of 304 cladding only (no pellets involved) in small deformation.

5) Performed the CIRFT test on the surrogate rod made of polycarbonate in large deformation.

6) Analyzed the hot cell CIRFT testing data on MOX SNF and other SNF tested under DOE sponsorship (see Sect. 3).

Two types of strain gages (Micro-Measurements, Raleigh, NC) were identified for this study, and the gage factors are given in Table 1. The setups of the surrogate rods with the strain gage mounted are shown in Fig. 6 and Fig. 7.

Table 1. Strain gages used in out-cell verification tests

Surrogate rod	Strain gage designation	Gage factor
SS304 surrogate rod	EA-06-250BF-350	2.055 +/- 0.5%
Polycarbonate rod	CEA-06-125UW-350	2.095+/-0.5%

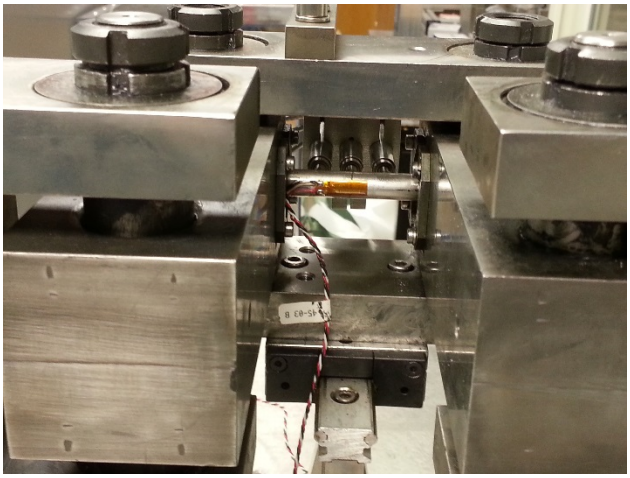

Fig. 6. Setup of SS304 surrogate rod with strain gage mounted in CIRFT testing.

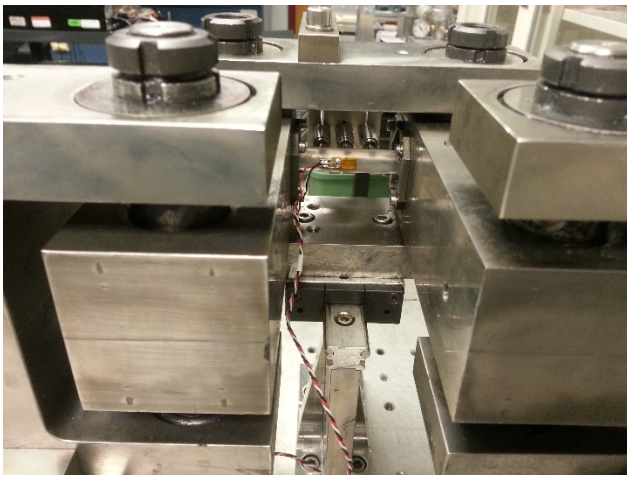

Fig. 7. Setup of polycarbonate surrogate rod with strain gage mounted in CIRFT testing.

1.3.5 Recommendation

It has been shown that the sensor spacing correction depends on the level of imposed displacement[10]. The corrected curvature based on disk-type probes agrees to a varying degree with the *EI*-based estimate in both small and large curvature measurements and with chisel-type probe measurements in the large curvature case. The corrected curvature-based strain was also shown to agree with the strain gage measurement, particularly at the small-to-intermediate level of displacement input.

There is some uncertainty associated with the contact of the probe against the rod during reversible bending testing. However, the proposed dynamic correction method of the LVDT probes is independent of contact spacing correction, as mentioned earlier. The identification of sensor spacing correction dynamically accounts for the changes and evolution of contacts. This effect is being investigated, the status of which will be reported in next performance period.

The proposed correction procedure will be applied to data analyses of the all CIRFT test results. The results of LMK, MOX, and HBR fuel analyses are presented in Sects. 2, 3, and 4, respectively.

2. CIRFT TESTING ON LIMERICK (LMK) BWR SNF

2.1 Overview of CIRFT Tests on LMK Fuel Rods

A specified number of LMK rod segments, each measuring 6 in. in length, were prepared from four parent LMK rods[11]. Endcaps were added to the rod segments using the vise mold designed for the larger outside diameter (OD) of the SNF rods. The endcap labels and segment IDs are provided in Table 2.

Table 2. CIRFT test number and segment labels of Limerick spent fuel rod

Spec	Endcap A*	Endcap B*	Segment ID	Note
LM01	LM1A	LM1B	574D-A	
LM02	LM2A	LM2B	575D-A	
LM03	LM3A	LM3B	575B-A	
LM04	LM4A	LM4B	575B-C	Endcaps misaligned. No test on this specimen.
LM05	LM5A	LM5B	574D-B	
LM06	LM6A	LM6B	574D-E	
LM07	LM7A	LM7B	575C-A	
LM08	LM8A	LM8B	575B-D	
LM09	LM9A	LM9B	574D-D	
LM10	LM10A	LM10B	575B-E	
LM11	LM11A	LM11B	575B-D	
LM12	LM12A	LM12B	575B-A	
LM13	LM13A	LM13B	575C-D	FY16
LM14	LM14A	LM14B	575C-B	FY16
LM15	LM15A	LM15B	575C-C	FY16
LM16	LM16A	LM16B	575D-E	FY16
LM17	LM17A	LM17B	575C-E	FY16

*Rod specimen is loaded into testing machine such that end caps A and B are on motor 2 and motor 1 sides, respectively.

Eleven specimens (LM1 to LM4, LM5 to LM12) were tested in FY 2015, and the data were analyzed using the procedure proposed in Sect. 1.3. The major results are provided in Table 3. The column headings of the table are defined as follows.

1) TN – test number
2) Spec – Specimen ID
3) ID – inside diameter of cladding
4) OD – outside diameter of cladding
5) Dia – diameter of pellet
6) Load – load amplitude at the loading point of U-frame

7) N – number of cycles accumulated or the cycles to failure

8) Fail – 1 as failure, and 0 as no failure

9) ma – mean of moment amplitude ($\Delta M/2$) based on de-noised monitoring data

10) ma_std – standard deviation of moment amplitude (4 in. or 101.60 mm loading arm) based on de-noised monitoring data

11) ka – mean of curvature amplitude ($\Delta\kappa/2$) based on corrected and de-noised monitoring data

12) ka_std – standard deviation of curvature amplitude based on corrected and de-noised monitoring data

13) km – mean of curvature extreme values based on corrected and de-noised monitoring data, $km = \max\{|\kappa_p|,|\kappa_v|\}$, where κ_p and κ_v are peak/valley values

14) km_std – standard deviation of curvature extremes based on corrected and de-noised monitoring data

15) R – mean of flexural rigidity

16) R_std – standard deviation of flexural rigidity

17) sa – mean of equivalent stress amplitude ($\Delta\sigma/2$) based on de-noised monitoring data

18) sa_std – standard deviation of equivalent stress amplitude based on de-noised monitoring data

19) ea – mean of equivalent strain amplitude ($\Delta\varepsilon/2$) based on corrected and de-noised monitoring data

20) ea_std – standard deviation of equivalent strain amplitude based on corrected and de-noised monitoring data

21) em – mean of strain extreme values based on corrected and de-noised monitoring data, $em = \max\{|\varepsilon_p|,|\varepsilon_v|\}$

22) em_std – standard deviation of strain extremes based on corrected and de-noised monitoring data

23) Lg2 – mean of half gauge length, Lg/2

24) Lg2_std – standard deviation of half gauge length

25) dh – mean of sensor spacing correction, Δh

26) dh_std – standard deviation of sensor spacing correction

Table 3a. Dynamic test results for LMK SNF rods – FY 2015

TN	Spec	Load	N	Fail	ma	ma_std	ka	ka_std	km	km_std
		N	cycles		Nm	Nm	m^1	m^-1	m^-1	m^-1
1	LM1	250	9.40E+03	1	23.426	0.087	0.901	0.027	1.007	0.027
2	LM2	125	1.71E+05	1	11.468	0.090	0.266	0.006	0.275	0.008
3	LM3	100	4.92E+05	1	9.016	0.081	0.243	0.008	0.258	0.011
5	LM5	85.	2.49E+05	1	7.570	0.074	0.165	0.008	0.205	0.013
6	LM6	75	1.79E+06	1	6.488	0.071	0.154	0.008	0.201	0.008
7	LM7	150	1.22E+05	1	13.930	0.085	0.347	0.005	0.362	0.009
8	LM8	75	4.70E+06	1	6.601	0.077	0.128	0.007	0.192	0.007
9	LM9	100	7.31E+05	1	9.058	0.077	0.216	0.004	0.226	0.007
10	LM10	200	5.20E+04	1	18.903	0.089	0.490	0.004	0.496	0.005
11	LM11	85	3.55E+05	1	7.657	0.111	0.162	0.007	0.194	0.010
12	LM12	70	7.58E+06	0	6.141	0.087	0.206	0.014	0.226	0.021

Table 3b. Dynamic test results for LMK SNF rods – FY 2015

TN	Spec	R	R_std	sa	sa_std	ea	ea_std	em	em_std	Lg2	Lg2_std	dh	dh_std
		Nm^2	Nm^2	MPa	MPa	%	%	%	%	mm	mm	mm	mm
1	LM1	26.017	0.809	179.649	0.667	0.515	0.015	0.575	0.015	43.766	0.767	0.279	0.182
2	LM2	43.120	0.891	88.227	0.691	0.151	0.004	0.156	0.005	44.250	0.634	-0.084	0.347
3	LM3	37.187	1.025	69.286	0.623	0.138	0.004	0.147	0.007	44.455	0.738	0.325	0.298
5	LM5	45.948	2.117	58.177	0.566	0.094	0.005	0.117	0.007	41.932	0.756	-1.436	0.577
6	LM6	42.226	2.287	49.862	0.548	0.088	0.005	0.114	0.005	40.157	0.749	-1.723	0.312
7	LM7	40.176	0.586	107.050	0.656	0.197	0.003	0.206	0.005	45.455	0.565	-0.426	0.190
8	LM8	51.567	2.504	50.733	0.590	0.073	0.004	0.109	0.004	42.342	0.890	2.568	0.338
9	LM9	41.880	0.736	69.615	0.590	0.123	0.003	0.129	0.004	43.120	0.698	0.206	0.215
10	LM10	38.563	0.336	145.272	0.684	0.279	0.002	0.282	0.003	46.986	0.528	0.355	0.173
11	LM11	47.437	2.009	58.848	0.856	0.092	0.004	0.110	0.006	41.396	0.757	-1.864	0.362
12	LM12	29.879	1.859	47.196	0.665	0.117	0.008	0.129	0.012	38.475	0.965	0.732	0.683

2.2 FY 2016 Tests and Results (Appendix A)

Five tests were conducted on specimens LM13 to LM17 during the reporting period. These specimens were tested in as-received condition just as in FY 2015. The load amplitude range used was also same as before, namely, from 8.64 to 30.48 Nm. The test at 8.64 Nm ran more than 3.37×10^6 cycles, and the specimen did not fail. That test was then stopped, and a new test was started at an increased amplitude.

2.2.1 Measurement/ Monitoring Data

The data sets for each of the dynamic tests, including measurement data and online monitoring data, were processed by using the procedure suggested in Sect. 2.

Results for each test are given in Appendix A. For each test:

1) The variations of curvature range, moment range, flexural rigidity, curvature peak/valley, and moment peak/valley are presented whenever they are available.
2) The curvature and moment plots are given for the beginning data block of a test session when the load reaches the designated level. The results for two test sessions are presented, namely, the first (tested to 1000 cycles) and last sessions.

3) Finally, the data based on online monitoring are presented, including the variations of curvature range, moment range, flexural rigidity, curvature peak/valley, and moment peak/valley as a function of the number of cycles or the cycles to failure.

For each cyclic test, two measurement data sets were obtained between test sessions. These measurements were made with small displacement amplitudes at 0.05 Hz. With such input, both moment and curvature varied or decreased along with the accumulated number of cycles. The obtained rigidities were generally higher than those from monitoring data, and the degree of changes was similar to those of monitoring data.

The flexural rigidity during the cyclic test was continuously either quite flat or showed a decreasing trend as the number of cycles increased. The rigidity of LM4 displayed a rise-and-fall variation pattern, but the degree of variation was limited. Meanwhile, no clear relation between rigidity and the number of cycles to failure could be seen. The correction observed for the curvature was not significant because of the small input, and the signal-to-noise ratio became smaller at the lower input. The amplitude of de-noised curvature was generally lowered compared to the original data, as expected.

2.2.2 Fatigue life

The major results of the dynamic tests are summarized in Table 4. The definitions given for the columns in Table 3 also apply to this table. Overall, the trends observed from FY 2015 tests were consistent with the FY 2016 data. For instance, fatigue life increased as the input level decreased; the effective half-gage length was limited to a range between 38 and 50 mm and increased as the amplitude of moment increased.

Plots based on the mean values of relevant quantities are shown in Fig. 8(a) to (d), where the circles represent the tests with failure and the circles with arrow designate the tests with no failure. The results from FY 2015 and FY 2016 (Table 3 and Table 4) are presented in order to obtain a comprehensive picture of SNF responses. The variation in fatigue life with amplitude was not continuous. A discontinuity or knee was observed near 7 Nm and 0.2 m^{-1} in the moment–N and curvature–N plots, respectively. For the SNF, these parameters correspond to 50 MPa of equivalent stress and 0.1% of equivalent strain. At the same time, curvature extreme values were generally higher than curvature amplitudes as expected, but the difference was small.

All of the failures of the specimens tested were observed to have occurred within the gage section, as illustrated in Fig. 9.

Table 4a. Dynamic test results for LMK SNF rods – FY16

TN	Spec	Load	N	Fail	ma	ma_std	ka	ka_std	km	km_std
		N	cycles		Nm	Nm	m^1	m^-1	m^-1	m^-1
13	LM13	250	2.10E+04	1	21.396	2.415	0.533	0.071	0.553	0.073
14	LM14	100	3.90E+05	1	9.048	0.082	0.198	0.008	0.228	0.010
15	LM15	100	4.41E+05	1	8.997	0.073	0.225	0.007	0.230	0.007
16	LM16	300	1.36E+04	1	28.560	0.168	0.654	0.008	0.679	0.014
17	LM17	85	3.37E+06	0	7.459	0.374	0.204	0.011	0.212	0.013
18	LM17	300	1.31E+04	1	28.063	0.131	0.853	0.006	0.863	0.011

Table 4b. cont'd

TN	Spec	R	R_std	sa	sa_std	ea	ea_std	em	em_std	Lg2	Lg2_std	dh	dh_std
		Nm^2	Nm^2	MPa	MPa	%	%	%	%	mm	mm	mm	mm
13	LM13	40.225	0.903	164.428	18.563	0.303	0.040	0.315	0.042	47.411	0.705	-0.138	0.143
14	LM14	45.659	1.768	69.535	0.632	0.113	0.005	0.130	0.006	44.092	0.781	-1.307	0.387
15	LM15	40.008	1.219	69.141	0.561	0.128	0.004	0.131	0.004	44.196	0.698	-0.148	0.585
16	LM16	43.672	0.480	219.490	1.295	0.372	0.005	0.386	0.008	50.296	0.440	-0.435	0.153
17	LM17	36.630	1.138	57.325	2.872	0.116	0.006	0.121	0.007	44.656	0.919	-0.849	0.338
18	LM17	32.913	0.252	215.671	1.004	0.485	0.003	0.491	0.006	47.420	0.331	1.211	0.092

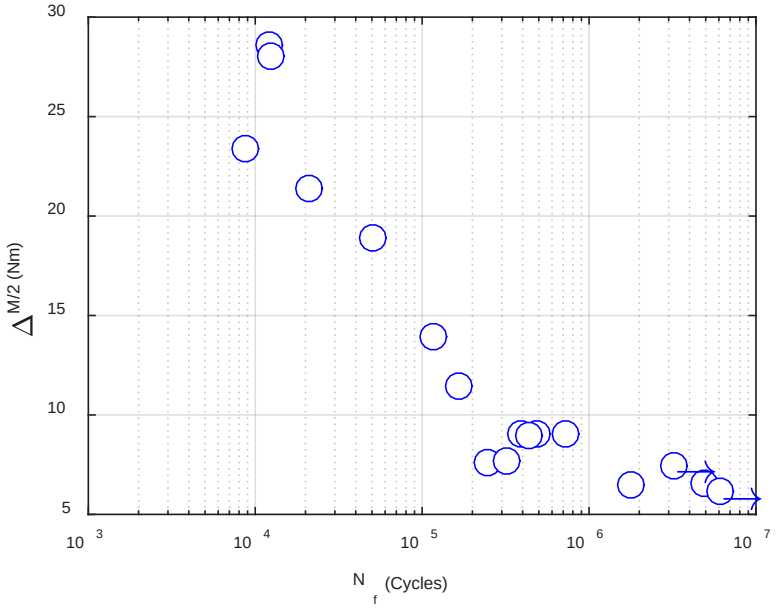
30
25
20
15
10
5
ΔM/2 (Nm)
10 3
10 4
10 5
10 6
10 7
N f (Cycles)

(a)

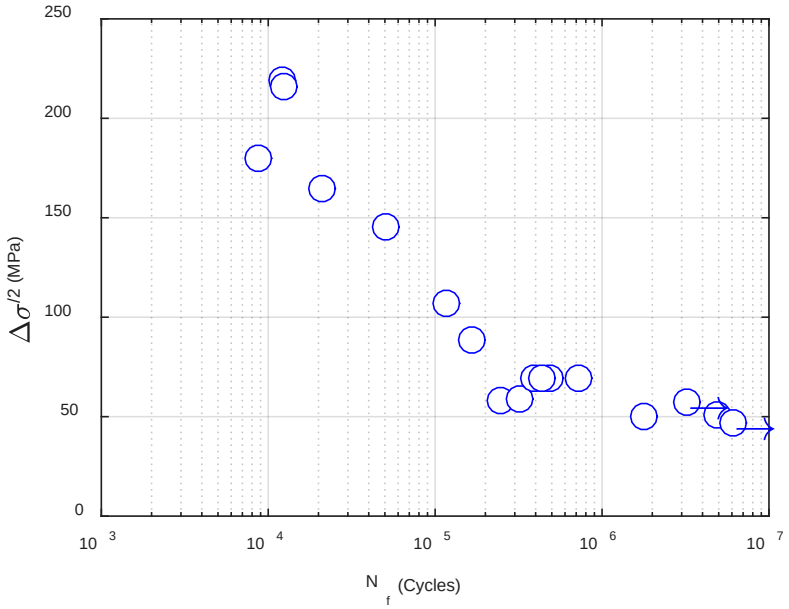
250
200
150
100
50
0
Δσ'/2 (MPa)
10 3
10 4
10 5
10 6
10 7
N f (Cycles)

(b)

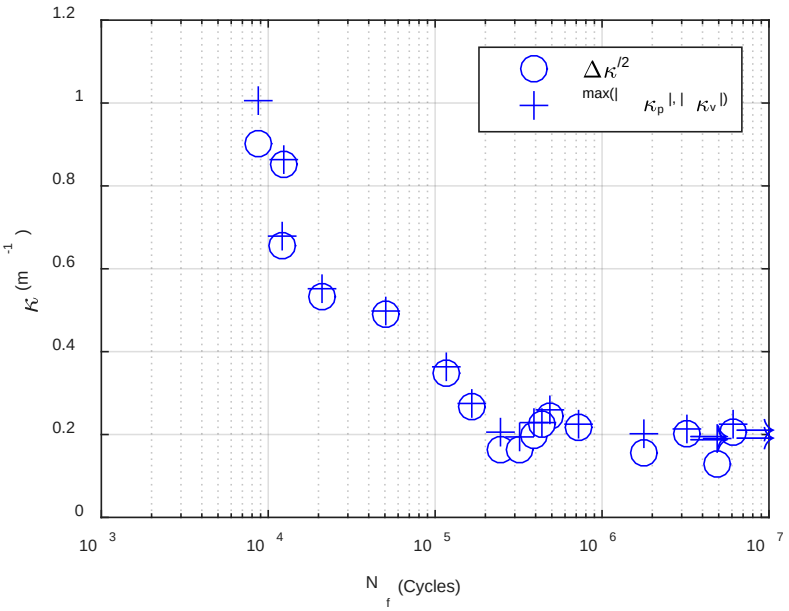

(c)

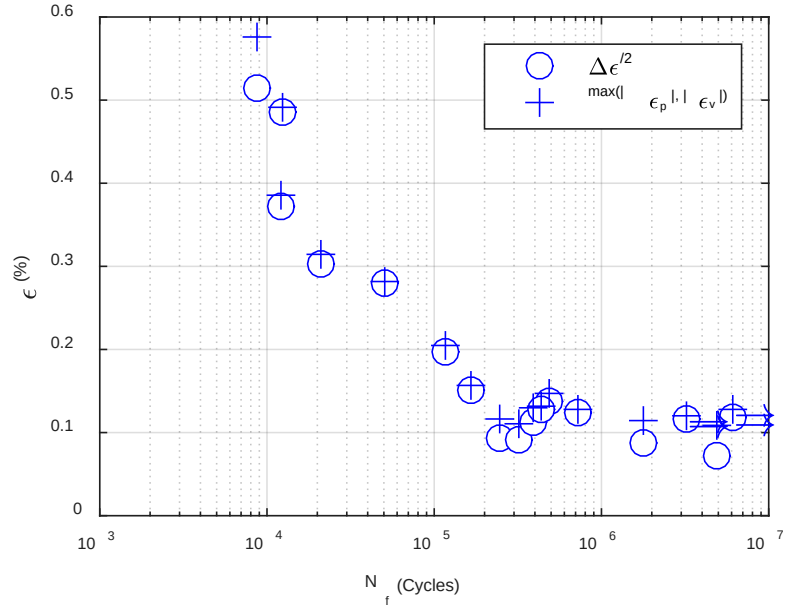

(d)

Fig. 8 (a) Moment amplitude, (b) stress amplitude, (c) curvature amplitude/ maximum, and (d) strain amplitude/ maximum as a function of cycles or cycles to failure.

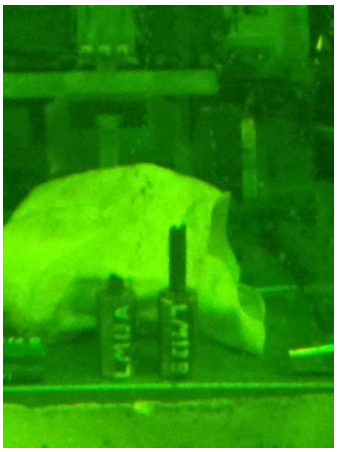

(a)

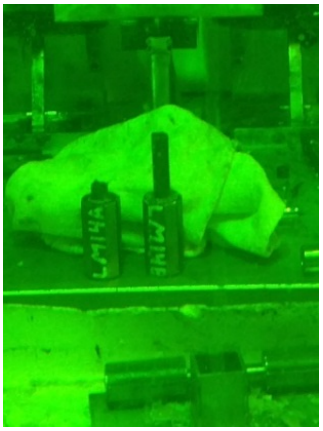

(b)

(c)

(d)

(e)

Fig. 9 Images showing failure modes or failure positions for specimens (a) LM13, (b) LM14, (c) LM15, (d) LM16, and (e) LM17.

3. CIRFT TESTING ON MOX FUEL

3.1 Overview of CIRFT Tests on MOX Fuel Rods

The segment ID and CIRFT labels of MOX fuel specimens are given in Table 5. Twelve tests were completed in FY 2014 and FY 2015. Of these, 10 dynamic tests were conducted with amplitudes from 5.08 to 15.24 Nm; all of the specimens failed, and the fatigue life ranged from 1.29×10^4 and 2.15×10^6 cycles. The measurement and monitoring data sets for these tests were processed using the procedure previously described, and the results are provided in Table 6.

Table 5. Specimen labels used for MOX SNF

CIRFT label	Endcap A	Endcap B	Segment ID	Note
MOX1	MOX-1A	MOX-1B	MOX-A-11	
MOX2	MOX-2A	MOX-2B	MOX-A-12	
MOX3	MOX-3A	MOX-3B	MOX-A-13	
MOX4	MOX-4A	MOX-4B	MOX-B-05	
MOX5	MOX-5A	MOX-5B	MOX-B-06	
MOX6	MOX-6A	MOX-6B	MOX-B-07	
MOX7	MOX-7A	MOX-7B	MOX-C-06	
MOX8	MOX-8A	MOX-8B	MOX-C-07	
MOX9	MOX-9A	MOX-9B	MOX-C-08	
MOX10	MOX-10A	MOX-10B	MOX-K-09	
MOX11	MOX-11A	MOX-11B	MOX-K-10	
MOX12	MOX-12A	MOX-12B	MOX-K-11	
MOX13	MOX-13A	MOX-13B	MOX-K-08	FY16
MOX14	MOX-14A	MOX-14B	MOX-C-09	FY16
MOX15	MOX-15A	MOX-15B	MOX-B-02	FY16
MOX16	MOX-16A	MOX-16B	MOX-K-16	FY16
MOX17	MOX-17A	MOX-17B	MOX-B-08	FY16
TH1	TH1-A	TH1-B	MOX-A-17	FY16
TH2	TH2-A	TH2-B	MOX-A-18	FY16
TH3	TH3-A	TH3-B	MOX-A-16	FY16
TH4	TH4-A	TH4-B	MOX-C-12	FY16
TH5	TH5-A	TH5-B	MOX-C-11	FY16
TH6	TH6-A	TH6-B	MOX-C-10	FY16

Table 6a. Dynamic test results for MOX SNF rods – FY 2014 and FY 2015

TN	Spec	Load	N	Fail	ma	ma_std	ka	ka_std	km	km_std
		N	cycles		Nm	Nm	m^1	m^-1	m^-1	m^-1
2	MOX2	100	3.70E+04	1	8.480	0.103	0.425	0.010	0.437	0.012
4	MOX4	50	2.15E+06	1	3.900	0.075	0.132	0.016	0.148	0.017
5	MOX5	60	4.49E+05	1	4.794	0.061	0.179	0.009	0.186	0.010
6	MOX6	50	5.42E+05	1	3.830	0.054	0.169	0.008	0.174	0.010
7	MOX7	150	1.55E+04	1	13.857	0.127	0.629	0.008	0.640	0.009
8	MOX8	125	1.29E+04	1	11.036	0.104	0.542	0.009	0.587	0.013
9	MOX9	75	8.98E+04	1	6.294	0.084	0.319	0.009	0.353	0.015
10	MOX10	100	3.85E+04	1	8.729	0.068	0.378	0.016	0.397	0.017
11	MOX11	100	4.23E+04	1	8.662	0.047	0.375	0.008	0.415	0.011
12	MOX12	100	4.23E+04	1	8.711	0.067	0.415	0.005	0.439	0.010

Table 6b. Cont'd

TN	Spec	R	R_std	sa	sa_std	ea	ea_std	em	em_std	Lg2	Lg2_std	dh	dh_std
		Nm^2	Nm^2	Mpa	MPa	%	%	%	%	mm	mm	mm	mm
2	MOX2	19.955	0.533	104.839	1.274	0.204	0.005	0.210	0.006	43.811	0.621	1.243	0.291
4	MOX4	29.939	3.703	48.216	0.932	0.063	0.008	0.071	0.008	40.575	2.133	-1.512	0.927
5	MOX5	26.797	1.235	59.265	0.758	0.086	0.004	0.089	0.005	43.766	1.027	-1.178	0.684
6	MOX6	22.744	1.021	47.347	0.662	0.081	0.004	0.084	0.005	43.751	0.867	0.059	0.395
7	MOX7	22.042	0.316	171.317	1.569	0.302	0.004	0.307	0.004	48.523	0.454	0.409	0.129
8	MOX8	20.377	0.282	136.440	1.282	0.260	0.004	0.282	0.006	49.223	0.484	0.441	0.144
9	MOX9	19.716	0.470	77.823	1.041	0.153	0.004	0.169	0.007	45.835	0.536	-0.505	0.190
10	MOX10	23.127	0.855	107.918	0.840	0.181	0.008	0.190	0.008	49.626	1.075	-0.428	0.276
11	MOX11	23.098	0.534	107.096	0.585	0.180	0.004	0.199	0.005	52.390	0.622	-1.036	0.260
12	MOX12	20.979	0.242	107.694	0.825	0.199	0.002	0.211	0.005	48.820	0.550	-0.678	0.182

3.2 FY 2016 Tests and Results (Appendix B)

Thirteen CIRFT tests were completed on MOX specimens in FY 2016. Six tests were conducted on the specimens that had been pre-treated by dropping them from a height of 12 in. with specimen laid horizontally, and the remaining seven tests used specimens that had been thermal treatment of 10 h at 400^{o}C, two cycles. The CIRFT tests were performed under amplitudes ranging from 7.62 to 12.70 Nm.

3.2.1 Measurement and Monitoring Data

The results for each test are given in Appendix B. The plots of the MOX fuels are similar to those of LMK fuels, including the variations in curvature range, moment range, flexural rigidity, curvature peak/valley, and moment peak/valley values.

The flexural rigidity of the rod specimens that were either dropped or annealed was lower than that of the as-received specimens. In most of the cases, the online monitoring generally demonstrated a steady or continuous variation in curvature in a cyclic test, depending on the moment amplitude and material condition. MOX14 was the exception, where a discontinuous rigidity variation was observed. Such a discontinuous response was apparently associated with the asymmetrical curvature increase of the specimen, in which an abrupt increase was seen near 10^4 cycles, as the specimen was approaching failure. For MOX15, a substantial negative shift in κ and a reduction in the κ range were observed after a restart of the test around 3.3×10^6 cycles.

3.2.2 Fatigue life

The results for the dynamic tests of MOX fuel in FY 2016 are summarized in Table 7. Definitions for the column heads are same as those given for LMK fuels in Table 3.

Plots based on the mean values of quantities are given in Fig. 10(a) to (d), where MOX1 represents the as-received specimens, MOX2 represents those subjected to 12 in. height drop, and MOX3 represents those that were thermal annealed. Fatigue life was shown to be affected by the condition of specimens. The 12 in. height drop seemingly reduces the fatigue life of SNF rods. At the same time, thermal annealing extends the fatigue life, which can be seen clearly from the two tests under 7.62 Nm as shown in Fig. 10(a).

Several images of the failed specimens that were pre-treated by the 12 in. drop are shown in Fig. 11, and specimens that had been thermally annealed are given in Fig. 12. Although a couple of specimens failed near the edge of endcaps, the failures were indeed taking place in the gage section of these specimens.

Table 7a. Dynamic test results for MOX SNF rods – FY 2016

TN	Spec	Load	N	Fail	ma	ma_std	ka	ka_std	km	km_std
		N	cycles		Nm	Nm	m^1	m^-1	m^-1	m^-1
13	MOX13	100	2.70E+04	1	8.725	0.059	0.450	0.007	0.466	0.011
14	MOX14	75	8.72E+04	1	6.190	0.091	0.668	0.172	1.456	1.160
15	MOX15	50	4.65E+06	0	3.842	0.074	0.184	0.028	0.216	0.011
16	MOX16	150	3.66E+03	1	13.209	1.656	0.986	0.273	1.007	0.345
17	MOX17	125	1.16E+04	1	11.104	0.951	0.700	0.663	0.768	0.960
18	MOX15	100	1.95E+04	1	8.474	0.065	0.439	0.005	0.445	0.008
19	TH1	100	5.70E+04	1	8.770	0.065	0.538	0.007	0.564	0.009
20	TH2	75	3.75E+06	0	6.234	0.107	0.353	0.009	0.380	0.013
21	TH3	125	1.51E+04	1	10.573	0.289	0.696	0.029	0.732	0.033
22	TH4	75	2.51E+06	1	6.284	0.150	0.399	0.025	0.438	0.027
23	TH5	125	2.76E+04	1	11.190	0.069	0.821	0.008	0.829	0.011
24	TH6	150	1.25E+04	1	13.391	0.157	0.812	0.014	0.832	0.018
25	TH2	125	5.73E+04	1	11.029	0.135	0.671	0.012	0.678	0.013

Table 7b. Cont'd

TN	Spec	R	R_std	sa	sa_std	ea	ea_std	em	em_std	Lg2	Lg2_std	dh	dh_std
		Nm^2	Nm^2	Mpa	MPa	%	%	%	%	mm	mm	mm	mm
13	MOX13	19.380	0.268	107.870	0.734	0.216	0.003	0.224	0.005	47.339	0.524	-0.040	0.190
14	MOX14	9.844	2.432	76.530	1.122	0.321	0.083	0.699	0.557	27.459	7.996	1.240	2.671
15	MOX15	21.440	3.764	47.501	0.917	0.088	0.013	0.104	0.005	43.138	3.120	0.741	1.512
15	MOX15	19.081	0.547	47.442	0.999	0.097	0.004	0.103	0.006	41.513	0.755	0.275	0.315
16	MOX16	13.822	1.700	163.310	20.479	0.473	0.131	0.483	0.165	48.167	0.841	0.188	0.275
17	MOX17	17.668	2.371	137.285	11.752	0.336	0.318	0.369	0.461	46.586	2.074	0.081	0.390
18	MOX15	19.310	0.165	104.774	0.804	0.211	0.002	0.214	0.004	47.594	0.516	0.170	0.192
19	TH1	16.292	0.186	108.425	0.800	0.258	0.004	0.271	0.004	49.023	0.443	0.738	0.145
20	TH2	17.656	0.350	77.071	1.322	0.170	0.004	0.182	0.006	48.349	0.802	-0.743	0.224
21	TH3	15.214	0.713	130.719	3.569	0.334	0.014	0.351	0.016	47.431	0.867	0.337	0.247
22	TH4	15.809	0.862	77.695	1.856	0.191	0.012	0.210	0.013	48.093	0.793	-0.217	0.790
23	TH5	13.638	0.151	138.354	0.847	0.394	0.004	0.398	0.005	47.979	0.372	0.297	0.136
24	TH6	16.504	0.394	165.556	1.942	0.390	0.007	0.399	0.008	49.765	0.385	-0.563	0.134
25	TH2	16.450	0.137	136.353	1.674	0.322	0.006	0.325	0.006	50.304	0.464	-0.366	0.109

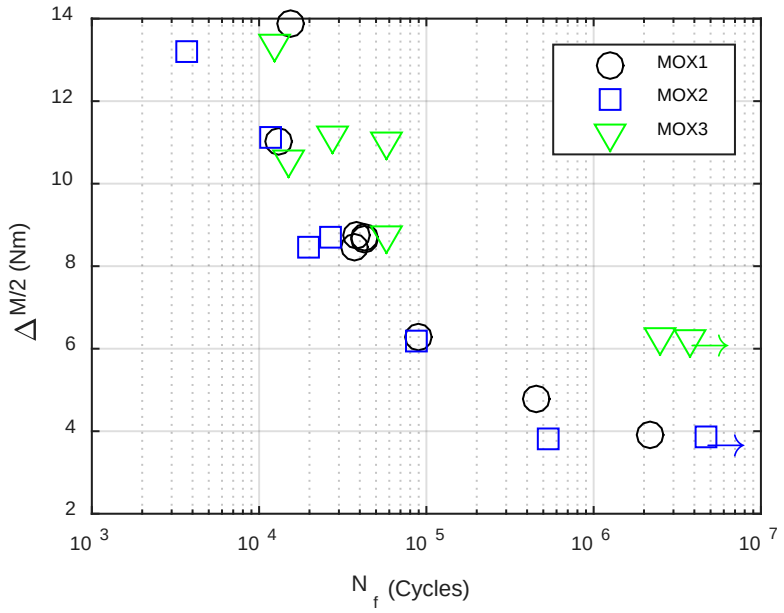
MOX1
MOX2
MOX3
Δ M/2 (Nm)
N f (Cycles)
14
12
10
8
6
4
2
10 3
10 4
10 5
10 6
10 7

(a)

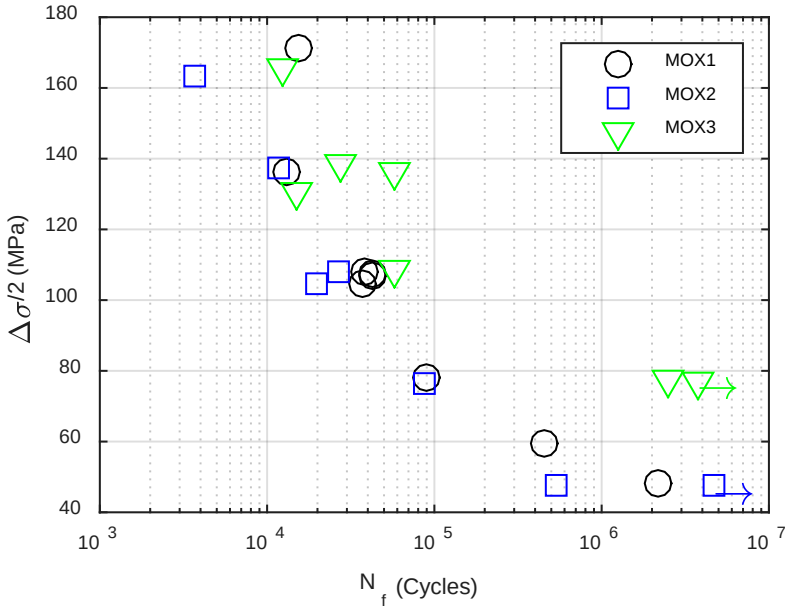
MOX1
MOX2
MOX3
Δσ/2 (MPa)
N f (Cycles)
180
160
140
120
100
80
60
40
10 3
10 4
10 5
10 6
10 7

(b)

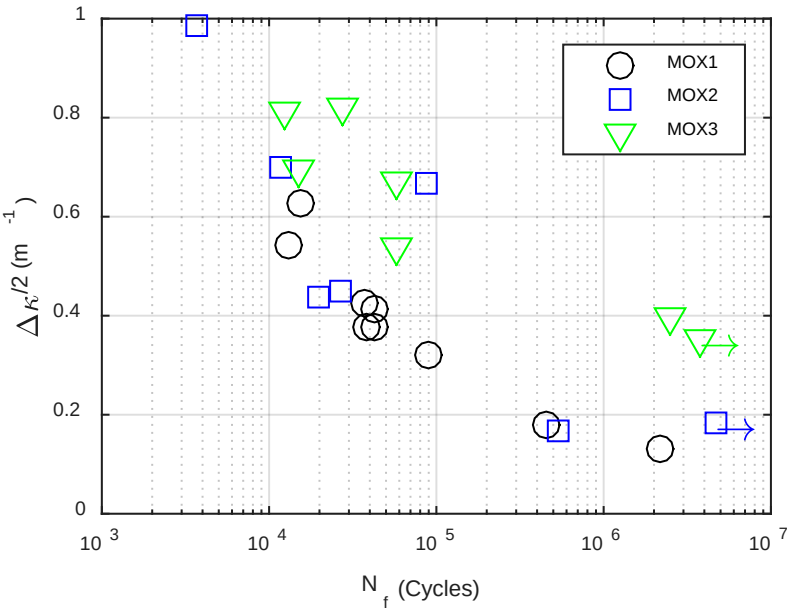

(c)

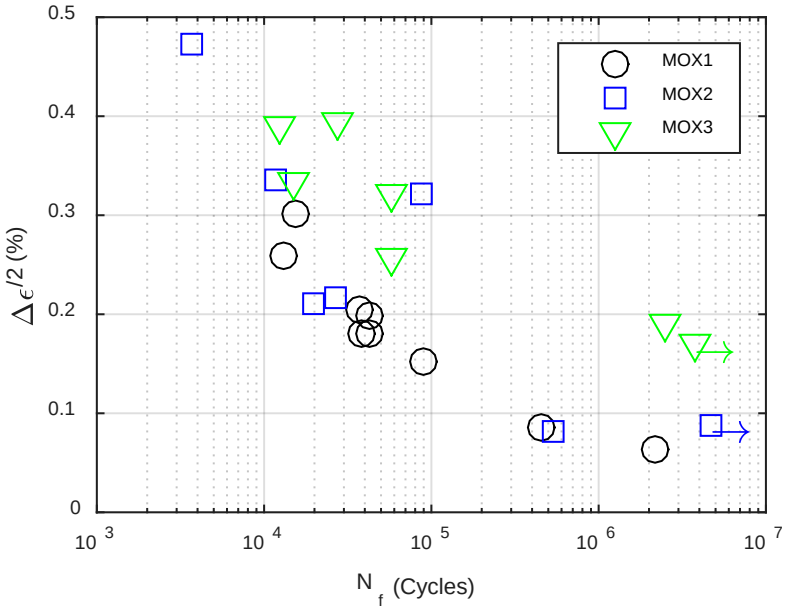

(d)

Fig. 10. (a) Moment amplitude, (b) stress amplitude, (c) curvature amplitude/ maximum, and (d) strain amplitude/ maximum as a function of cycles or cycles to failure. MOX1 – as received; MOX2 – 12 in. drop; MOX3 – thermal annealed.

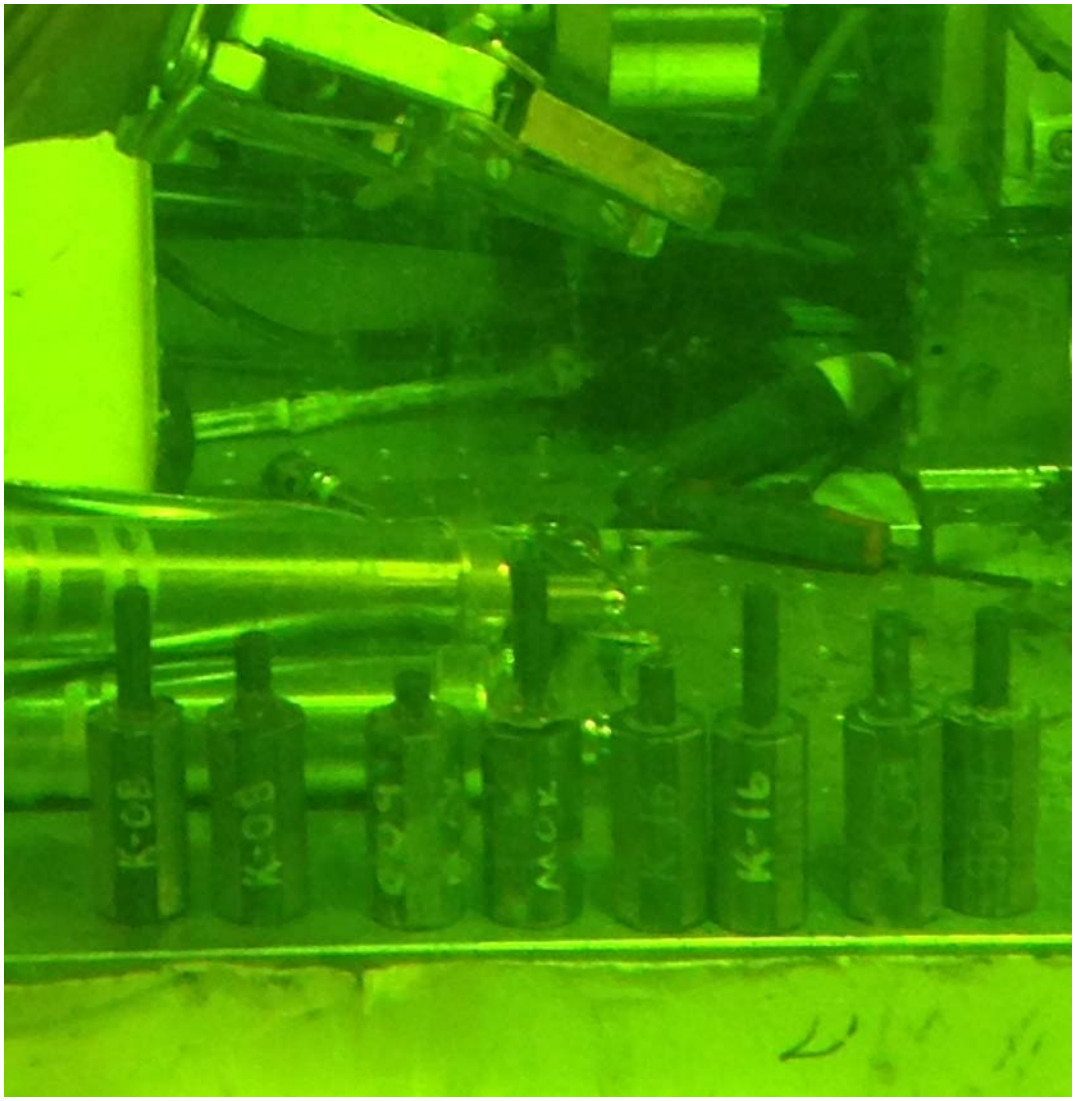

Fig. 11. Images of MOX fractured samples with 12 in. drop, MOX13 (K-08), MOX14 (C-09), MOX15 (B-02), and MOX16 (K-16).

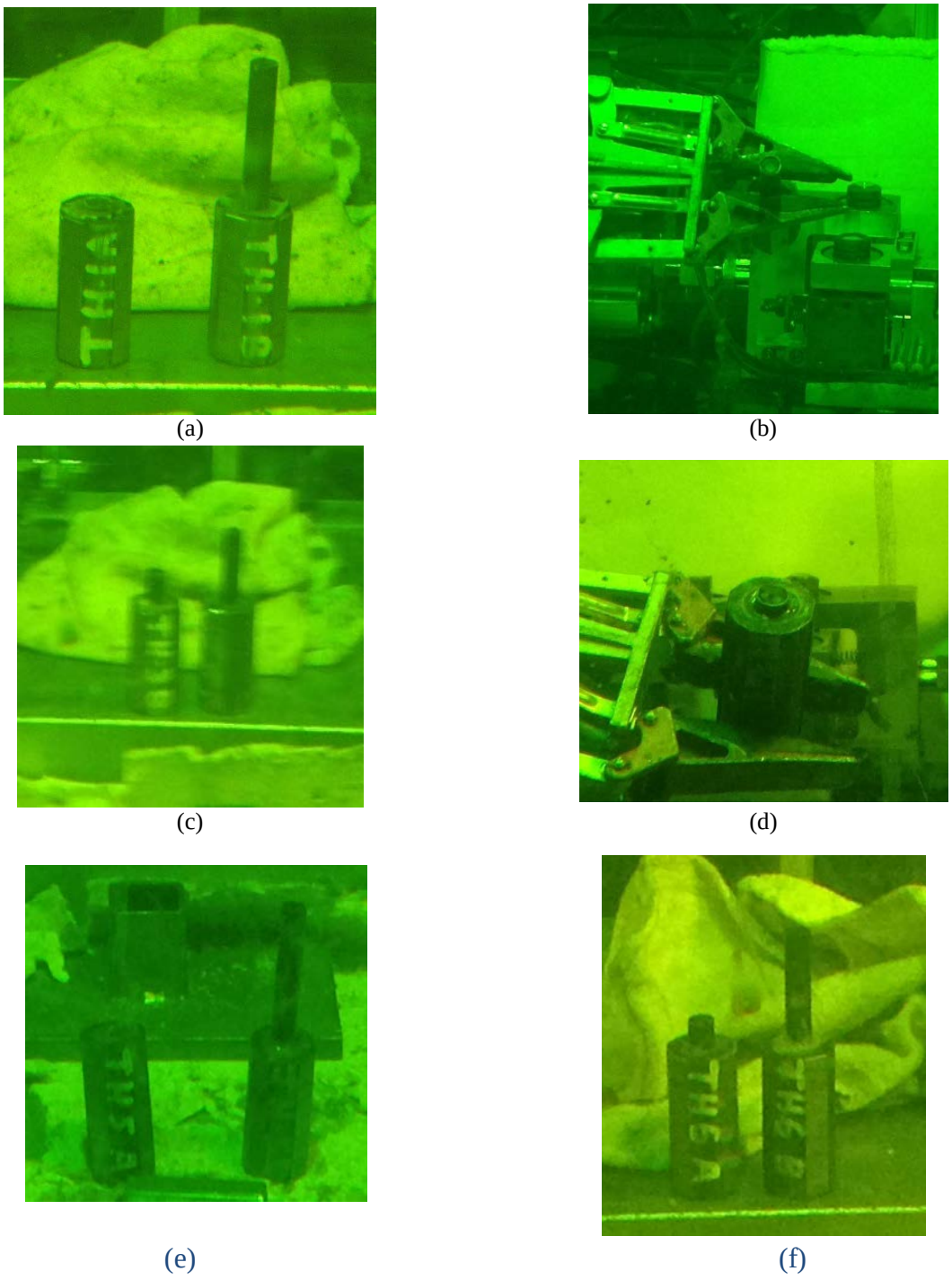

(a) (b) (c) (d) (e) (f)

Fig. 12. Images showing the failure positions of (a) TH1, (b) TH2, (c) TH3, (d) TH4, (e) TH5, and (f) TH6.

4. CIRFT TESTING ON H. B. Robinson (HBR) FUEL for Hydride Reorientation Study

4.1 Overview of CIRFT Tests and Results on HBR Fuel Rods

Rod segments, measuring 6 in. in length, for CIRFT tests were prepared from five high-burnup (HBU) HBR SNF rods. Specimen labels and corresponding segment IDs are given in Table 8.

ORNL completed 24 tests in FY 2013 and FY 2014. Fifteen tests were dedicated to dynamic testing conditions with amplitudes ranging between 5.08 and 35.56 Nm. Several tests run at amplitudes below 8.89 Nm ran over tens of millions of cycles, and the specimens did not show any sign of failure, so these tests were stopped.

Table 8. Specimen labels used for HBR SNF

Spec ID	Endcap A	Endcap B	Seg. ID	Note
Demo1	Demo1-A	Demo1-B	606B2	
S3	S3-A	S3-B	605D1F	
S1	S1-A	S1-B	606C3C	
S2	S2-A	S2-B	605D1E	
Dcal	Dcal-A	Dcal-B	609C5	
DL1	DL1-A	DL1-B	607C4B	
DL2	DL2-A	DL2-B	608C4B	
DL3	DL3-A	DL3-B	605C10A	
DM2	DM2-A	DM2-B	605D1B	
DM1	DM1-A	DM1-B	605D1C	
DH1	DH1-A	DH1-B	609C4	
DH2	DH2-A	DH2-B	609C3	
DM3	DM3-A	DM3-B	606C3E	
DH3	DH3-A	DH3-B	609C7	
S5	S5-A	S5-B	606C3A	
R1	R1-A	R1-B	607C4A	
R2	R2-A	R2-B	608C4A	
R3	R3-A	R3-B	606B3E	
R4	R4-A	R4-B	606B3D	
R5	R5-A	R5-B	606B3C	
HR1	HR1-A	HR1-B	607D4C	FY16
HR2	HR2-A	HR2-B	607D4A	FY16
HR3	HR3-A	HR3-B	608D4A	FY16
HR4	HR4-A	HR4-B	608D4C	FY16

4.2 FY 2016 Test Results (Appendix C)

Four CIRFT tests were completed on the HBR specimens with radial hydride treatment (RHT, 120 MPa hoop stress, 170 to 400°C, five cycles) in FY 2016. Amplitudes ranging from 10.16 and 16.26 Nm were tested. One of the HBR RHT specimens (HR2) was tested under the following static conditions prior to dynamic testing: (1) six cycles of unidirectional bending with relative peak displacement 12 mm at U-frame loading points and (2) four cycles of fully reversed bending with relative peak/valley displacement +/-12 mm. This specimen apparently survived the static loading without failure and was then tested under dynamic loading, as will be discussed in the following. Due to a welded end-cap leak, only thermal heat treatment was applied to the HR4 sample.

The sample preparation for the hydride reorientation (HR) project is detailed below.

- The HBU HBR fuels under simulated drying operation conditions of the SNF were used for HR testing study. Based on out-of-cell benchmark HR tests with hydrided HBR cladding, four in-cell HR tests were conducted with HBU HBR fuel samples at ≈145 MPa at 400°C.
- The HBR fuel samples for HR tests were prepared in the irradiation fuel examination laboratory. After the samples were sectioned into 6-in.-long pieces, the surface oxide layer and fuels were removed from both ends to a depth of approximately 0.5 in. End caps were welded at both ends, and the HBR fuel specimens were then pressurized with argon gas at a maximum hoop stress level of 145 MPa and a target hold temperature T = 400°C. However, thermal cycling was performed to increase the radial hydrides. After fabrication, the specimens were placed in a holder within the furnace for heating to a target temperature of 400°C, held for 3 hours, cooled at 1°C/min to 170°C, and then heated at 1°C/min to a target hold temperature of 400°C again for five cycles. The samples were furnace cooled from 170°C to room temperature for the last cycle. All in-cell tests had the same temperature profiles. Figure 13 shows the temperature history of the first in-cell HR test, HR1, with a HBU HBR sample.

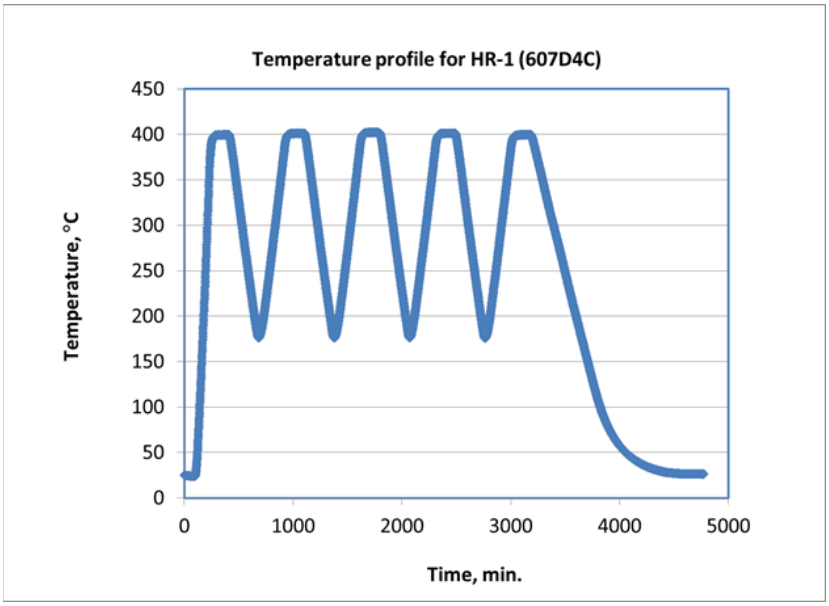

Fig. 13. Sample temperature as a function of time for In-cell HR Test HR-1.

- The hydride-reoriented samples were sent to Work Station 12, where the CIRFT tests were performed at room temperature to evaluate the materials performance after the HR tests. After the CIRFT tests were completed, the specimens were sent to Work Station 3, where the post-hydride-

reoriented sample was examined to verify whether the radial hydrides had been generated. Figure 14 shows the hydride morphology of hydride-reoriented sample HR1. The hydrogen concentration of this sample was about 360–400 wppm. The MET mount specimen was sectioned at the midplane of a 6-in.-long sample. Although the in-cell HR test conditions were the same as the out-of-cell test HR-HBR#2 and the hydrogen concentration of these two samples were compatible, the morphology of HBU sample HR1 was quite different from hydrided sample HR-HBR#2. For the unirradiated sample, the circumferential hydrides were uniformly distributed across the wall, and the maximum length of its radial hydrides was about 50–60 μm. For HBU samples, the radial hydrides were mainly distributed near the inner surface and the circumferential hydrides are mostly seen near the outer surface. The length of the radial hydride of the HBU sample ,Fig. 14(a), was also much longer than the unirradiated sample, Fig. 149(b).

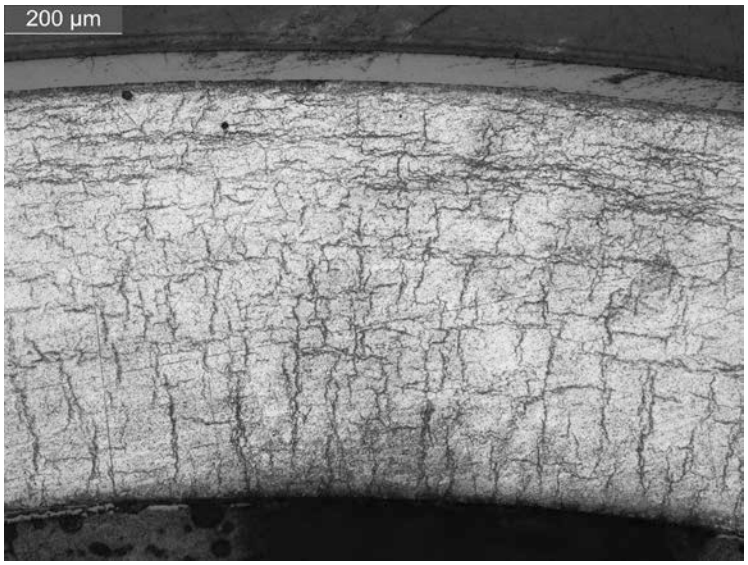

(a)

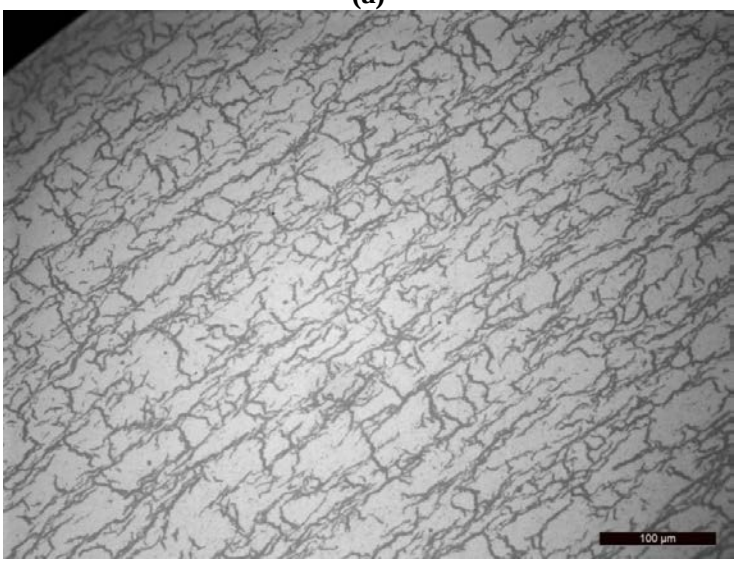

(b)

Fig. 14. (a) High magnification micrograph showing radial hydrides of Sample HR-1 (H ≈ 360-400 ppm). The HBU HBR specimen was pressurized to 145 MPa at 400°C with five thermal cycles. (b) High magnification micrograph showing radial hydrides of Sample HR-HBR#2 (H ≈ 286 ppm). The specimen was sectioned at the midplane of a 6-in.-long sample.

4.2.1 Measurement and Monitoring Data

The results for each test are given in Appendix C. The plots of HBR fuels are similar to those of LMK fuels, including the variations of curvature range, moment range, flexural rigidity, curvature peak/valley, and moment peak/valley values.

The flexural rigidity of the rod specimens treated by hydride re-orientation was shown to be much lower than that of as-received specimens under equivalent amplitude. For example, under the same amplitude of 100 N, the rigidity of the RHT specimen (HR3) was only about 57% that of the as-received specimen (DL3). The variation of rigidity during a cyclic test was generally pretty continuous. In HR3, a sudden drop was observed prior to the failure.

4.2.2 Fatigue Life

The results for the dynamic tests of HBR fuel in FY 2016 are summarized in Table 9. Again, definitions of the column heads are same as those for LMK fuels in Table 3.

The plots based on the mean values of quantities are given in Fig. 15 (a) to (d), where HBR1 represents the as-received specimen and HBR2 represents the specimen after radial hydride treatment (RHT). Note that the data of as-received HBR specimens were based on the original analysis method; namely, no correction was applied. It has been shown that the RHT reduces the fatigue life of SNF rods, as can be seen from the tests around 15 Nm. It was further observed that for HR2, as indicated by the arrow, there was an additional fatigue life reduction. Such reduction obviously resulted from the large-deformation static loading before the dynamic cyclic loading.

Several images on the failed specimens that were pre-treated by the thermal annealing are given in Fig. 16. The failures of these specimens were in gage section, and in two of them, the failure was taking place on a pellet-to-pellet interface (PPI).

Table 9a. Dynamic test results for HBR SNF rods – FY 2016

TN	Spec	Load	N	Fail	ma	ma_std	ka	ka_std	km	km_std
		N	cycles		Nm	Nm	m^1	m^-1	m^-1	m^-1
25	HR1	150	4.19E+04	1	15.152	0.549	0.517	0.016	0.527	0.019
26	HR2	160	9.47E+03	1	14.702	0.806	0.478	0.121	0.511	0.205
27	HR3	100	2.44E+05	1	8.982	0.066	0.267	0.005	0.291	0.009
28	HR4	160	5.47E+04	1	14.759	0.089	0.394	0.008	0.421	0.009

Table 9b. Cont'd

TN	Spec	R	R_std	sa	sa_std	ea	ea_std	em	em_std	Lg2	Lg2_std	dh	dh_std
		Nm^2	Nm^2	Mpa	MPa	%	%	%	%	mm	mm	mm	mm
25	HR1	29.329	0.775	128.788	4.666	0.278	0.009	0.284	0.010	44.733	0.565	1.329	0.197
26	HR2	31.567	3.256	124.964	6.848	0.257	0.065	0.275	0.110	50.657	1.593	-0.174	0.372
27	HR3	33.659	0.602	76.342	0.560	0.144	0.003	0.157	0.005	43.368	0.643	-1.649	0.252
28	HR4	37.497	0.593	125.449	0.755	0.212	0.004	0.227	0.005	45.977	0.578	1.206	0.201

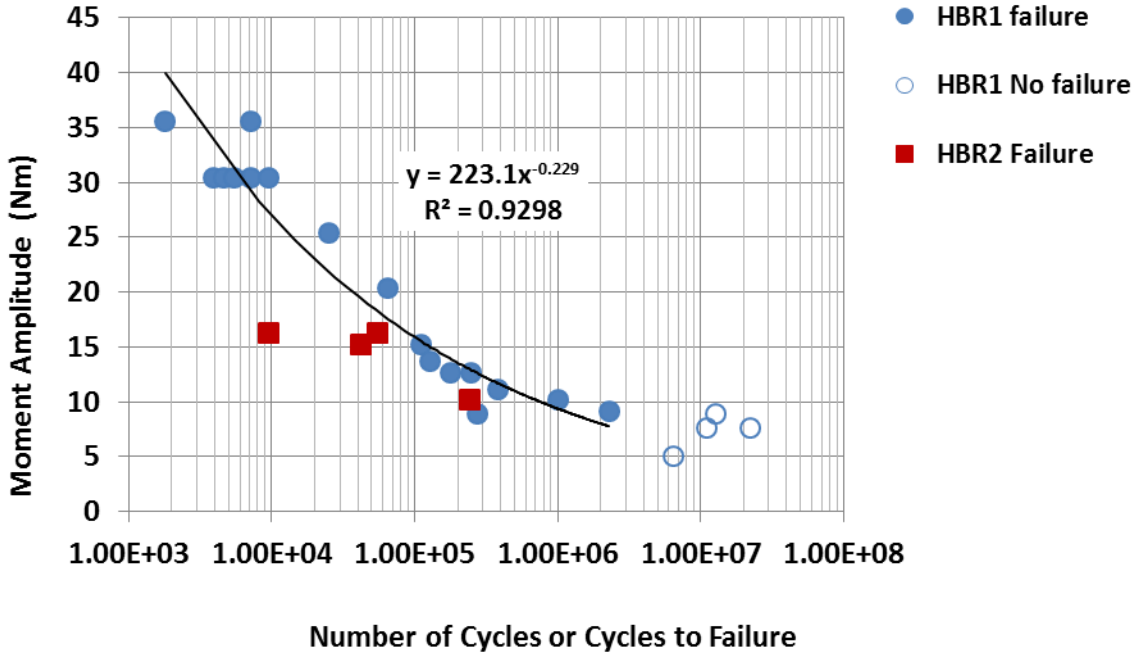
45
40
35
30
25
20
15
10
5
0
Moment Amplitude (Nm)
y = 223.1x-0.229
R² = 0.9298
1.00E+03
1.00E+04
1.00E+05
1.00E+06
1.00E+07
1.00E+08
Number of Cycles or Cycles to Failure
HBR1 failure
HBR1 No failure
HBR2 Failure

(a)

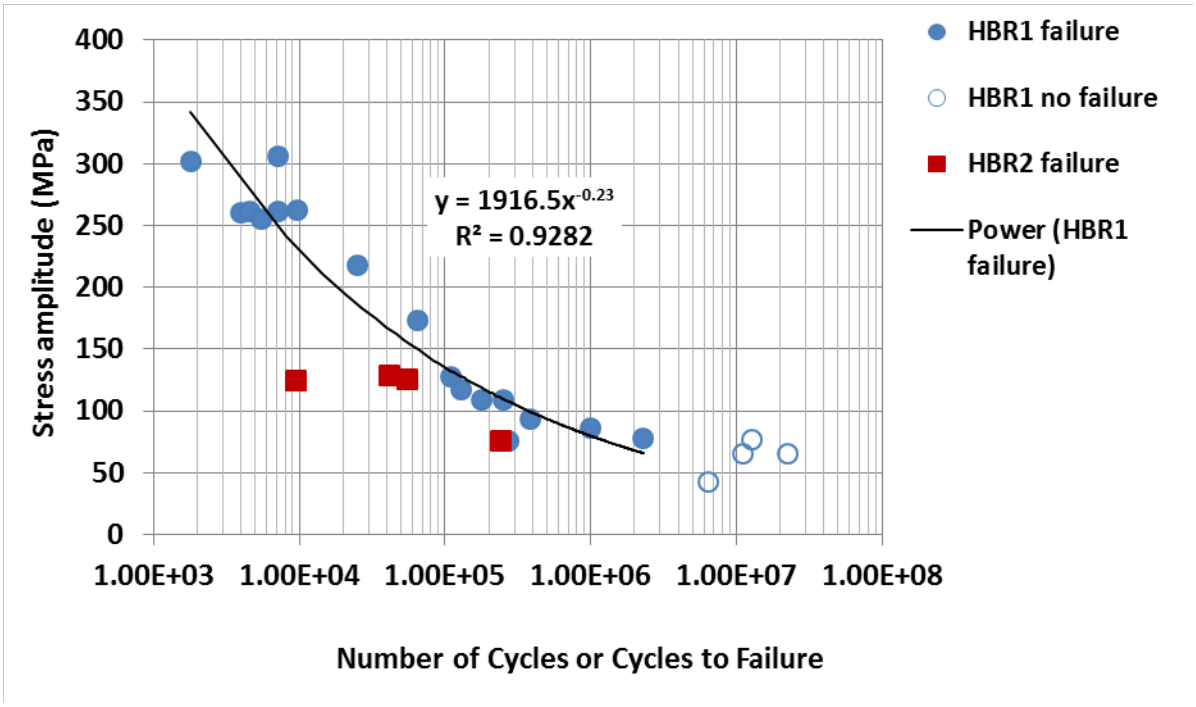
400
350
300
250
200
150
100
50
0
Stress amplitude (MPa)
y = 1916.5x-0.23
R² = 0.9282
1.00E+03
1.00E+04
1.00E+05
1.00E+06
1.00E+07
1.00E+08
Number of Cycles or Cycles to Failure
HBR1 failure
HBR1 no failure
HBR2 failure
Power (HBR1 failure)

(b)

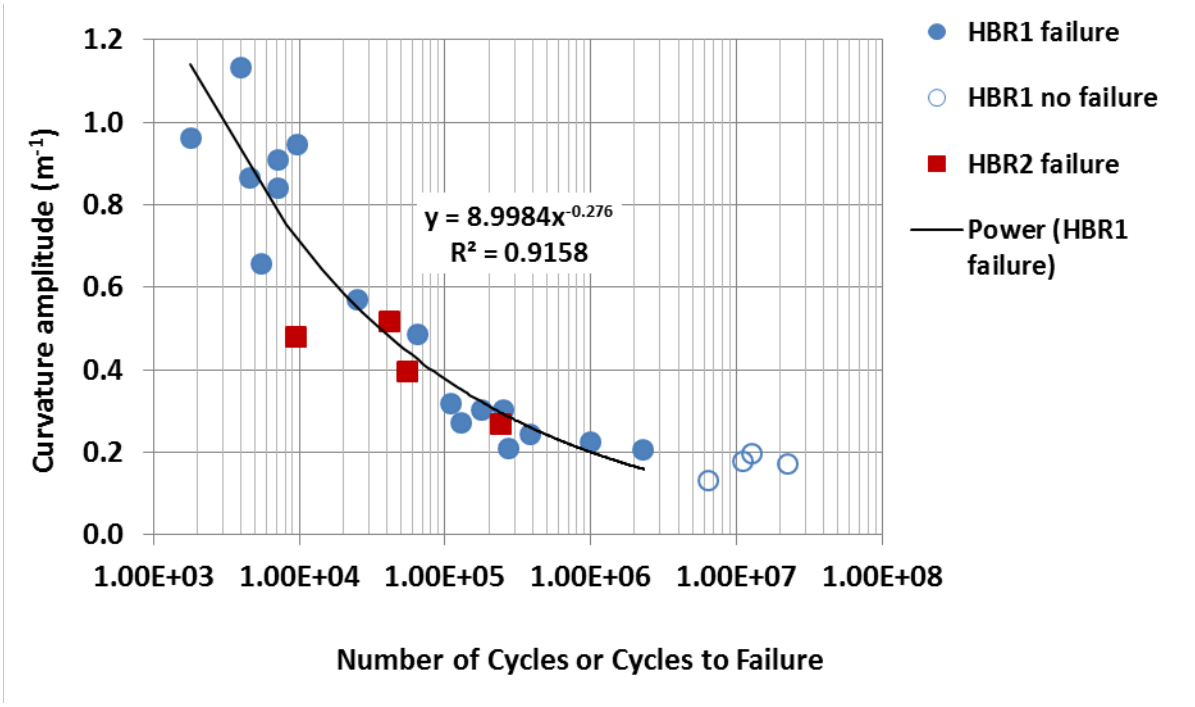

(c)

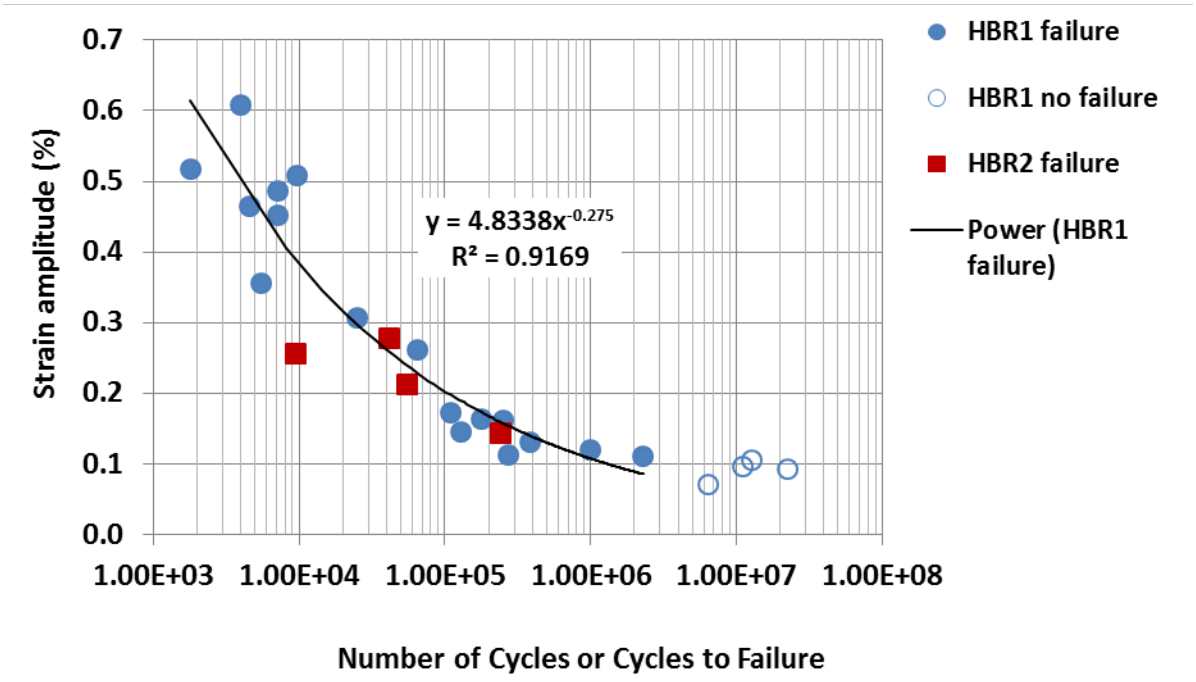

(d)

Fig. 15. (a) Moment amplitude, (b) stress amplitude, (c) curvature amplitude, and (d) strain amplitude rigidity as a function of cycles or cycles to failure.

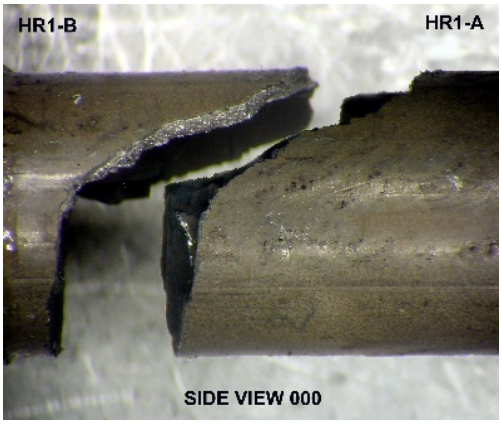
HR1-B
HR1-A
SIDE VIEW 000

(a)

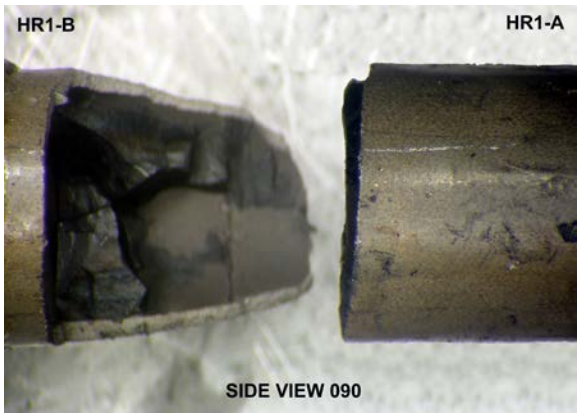
HR1-B
HR1-A
SIDE VIEW 090

(b)


HR1-A
END VIEW

(c)

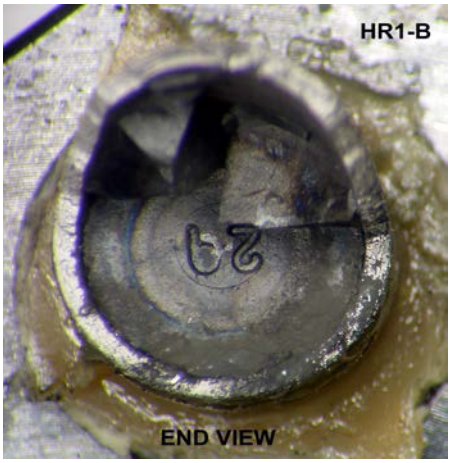
HR1-B
END VIEW

(d)

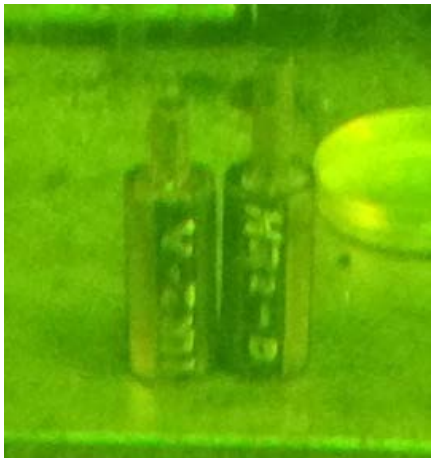

(e)

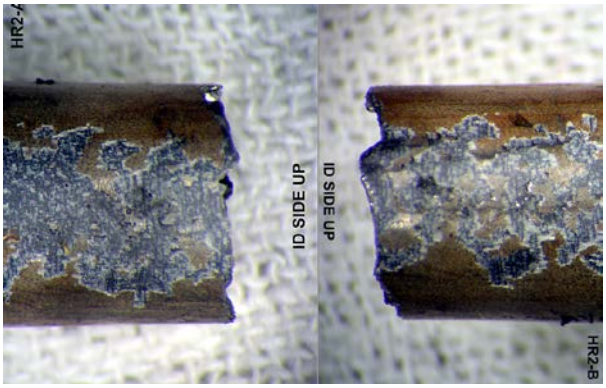
ID SIDE UP
ID SIDE UP
HR2-B

(f)

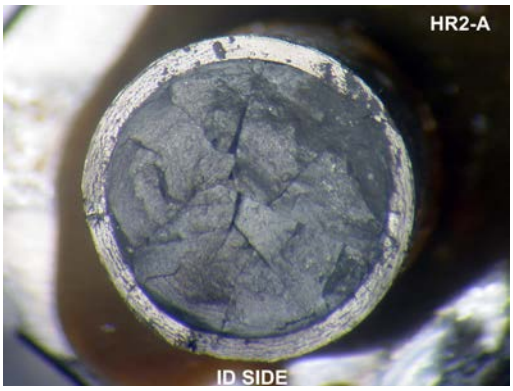
HR2-A
ID SIDE

(g)

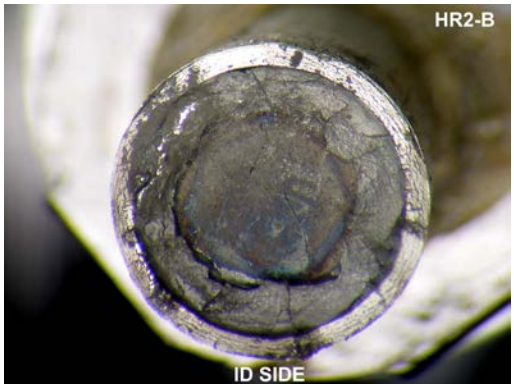
HR2-B
ID SIDE

(h)

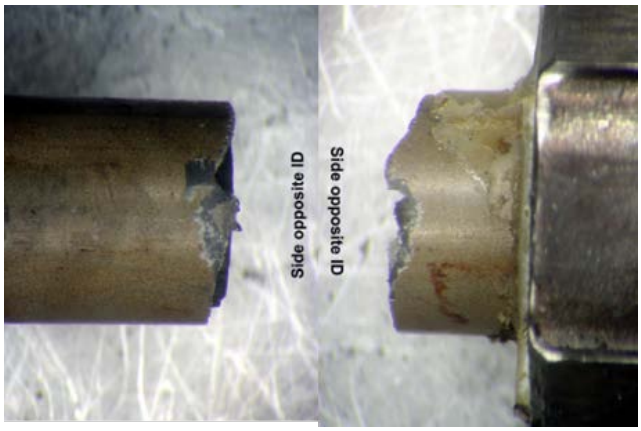
Side opposite ID
Side opposite ID

(i)

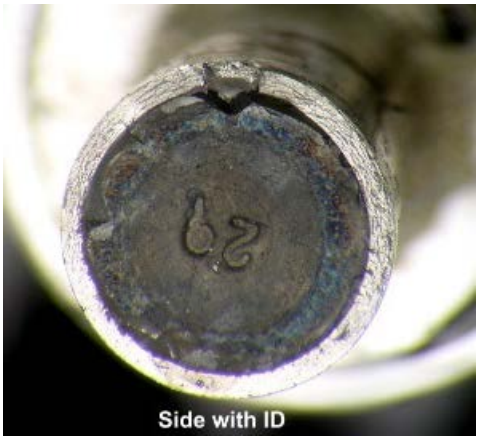
Side with ID

(j)


HR-4A
B-4YK

(k)

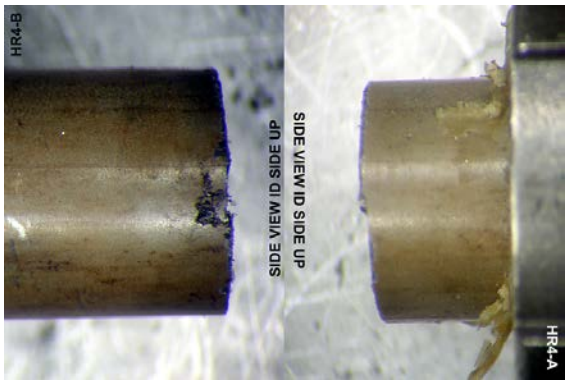
HR4-B
SIDE VIEW ID SIDE UP
SIDE VIEW ID SIDE UP
HR4-A

(l)

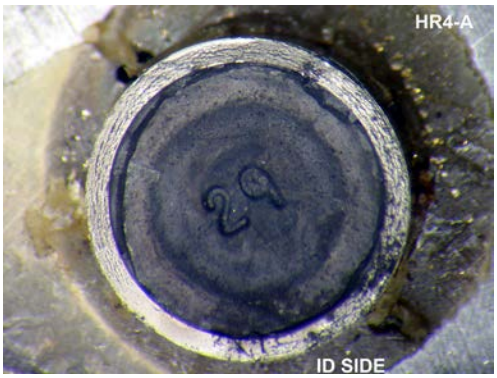

(m)

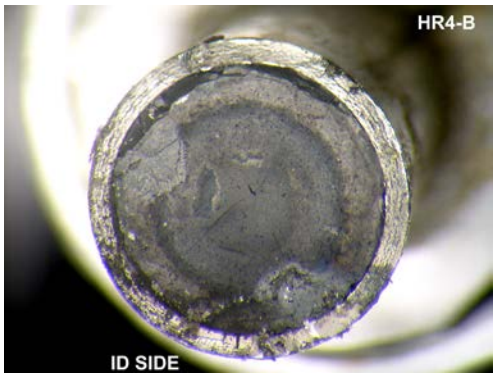

(n)

Fig. 16. Images showing the failure modes for (a) (b) (c) (d) HR1, (e) (f) (g) (h) HR2, (i) (j) HR3, and (k) (l) (m) (n) HR4.

5. DISCUSSION AND REMAINING ISSUES

5.1 Fatigue Life of SNF

The variations in fatigue life are given in Fig. 17 in terms of moment, equivalent stress, curvature, and equivalent strain for the tested SNFs, where the following designations are used.

1) LMK – as-received
2) MOX1 – as-received
3) MOX2 – 12 in. height drop treatment
4) MOX3 – thermal annealing treatment
5) HBR1 – as-received
6) HBR2 – radial hydride treatment

The equivalent stress indeed collapsed the data points from all of the SNFs into a single zone. A detailed examination revealed that, at same stress level, fatigue lives display a descending order as follows: HBR, LMK, MOX. If looking at the strain, LMK fuel has a slightly longer fatigue life than HBR, but the difference is subtle.

The knee point of endurance limit in the curve of moment and curvature or equivalent quantities is more clearly defined for LMK and HBR fuels.

The treatment affects the fatigue life of specimens. Both the 12 in. drop and RHT have a negative impact on the fatigue life of specimens. The effect of the thermal annealing on MOX fuel rod was relatively small at the higher amplitude but became significant in the low amplitude of moment. Thermal annealing tends to extend the fatigue life of specimens of the MOX fuel rod. However, for HR4 specimen testing of the HBR rod, the thermal annealing treatment shows a negative impact on the fatigue life of the HBR rod.

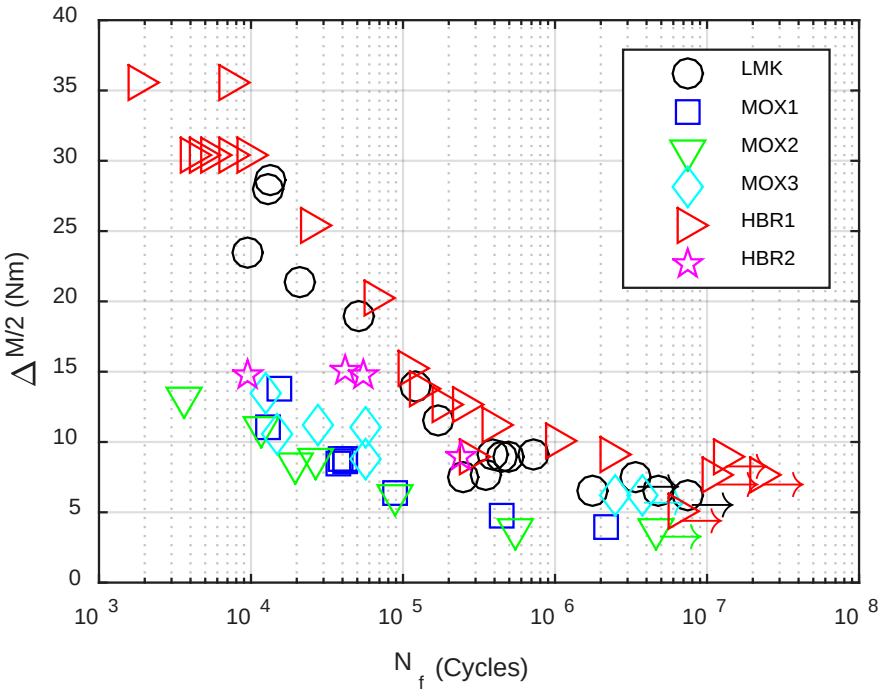
LMK
MOX1
MOX2
MOX3
HBR1
HBR2
ΔM/2 (Nm)
N f (Cycles)

(a)

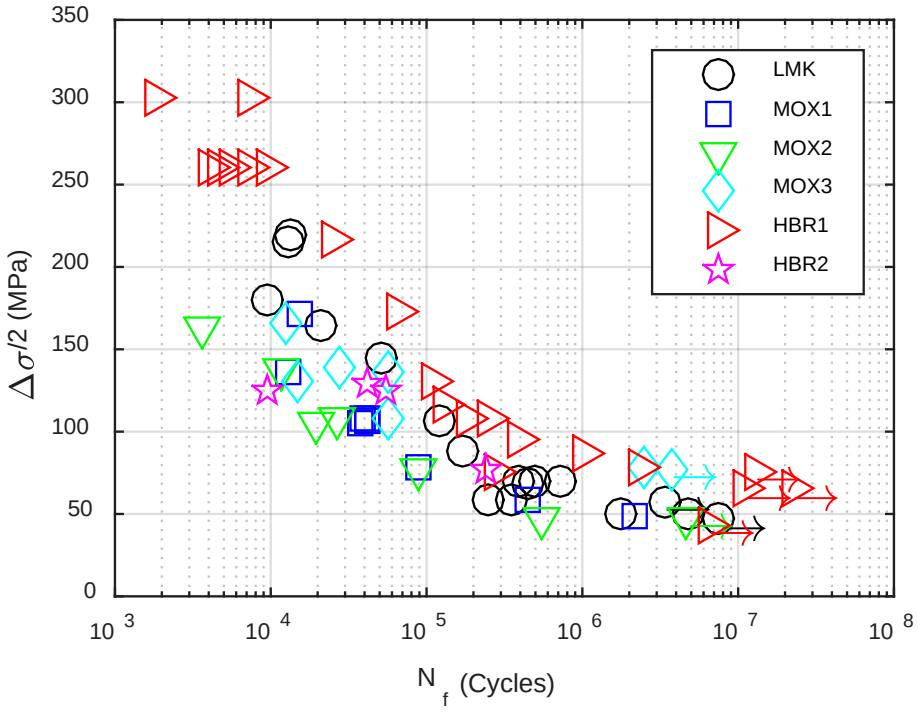
LMK
MOX1
MOX2
MOX3
HBR1
HBR2
Δσ/2 (MPa)
N f (Cycles)

(b)

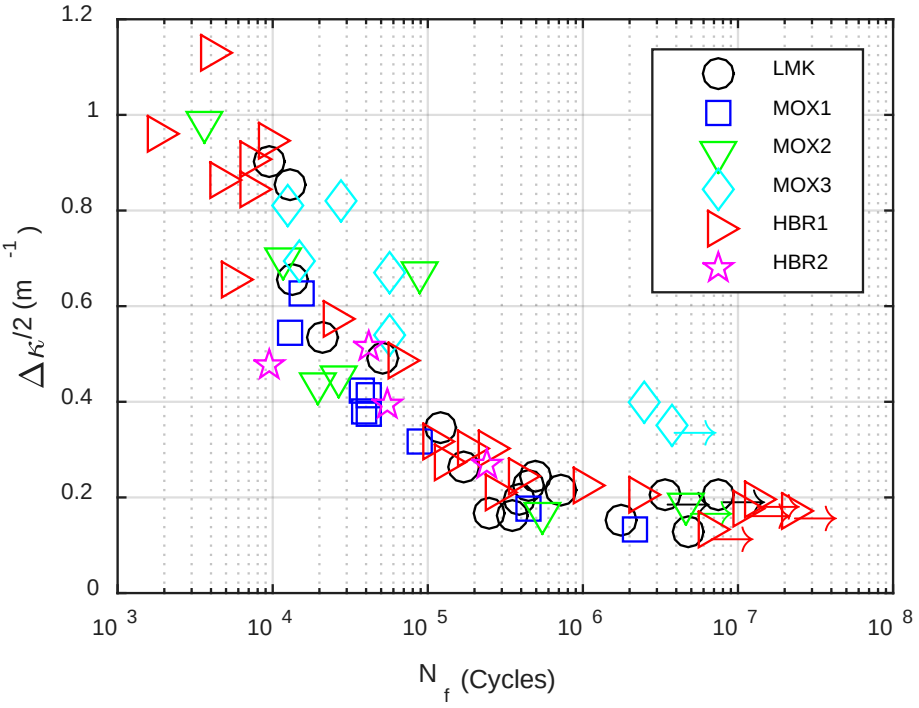
1.2
1
0.8
0.6
0.4
0.2
0
$\Delta\kappa^{1/2}$ (m $^{-1}$)
10^3
10^4
10^5
10^6
10^7
10^8
N_f (Cycles)
LMK
MOX1
MOX2
MOX3
HBR1
HBR2

(c)

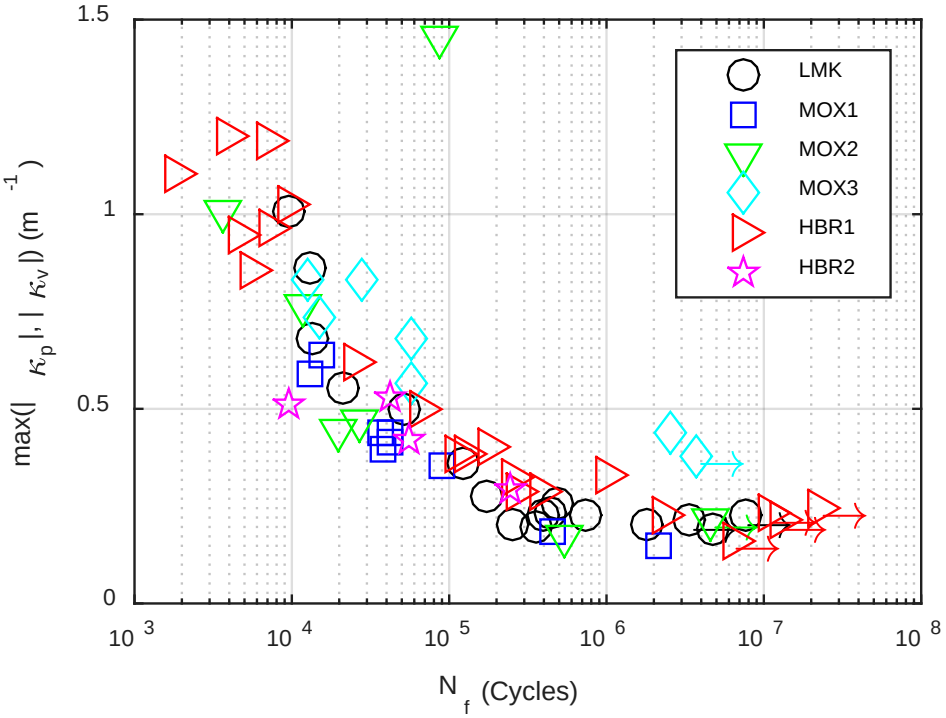
1.5
1
0.5
0
max(| κ_p |, | κ_v |) (m $^{-1}$)
10^3
10^4
10^5
10^6
10^7
10^8
N_f (Cycles)
LMK
MOX1
MOX2
MOX3
HBR1
HBR2

(d)

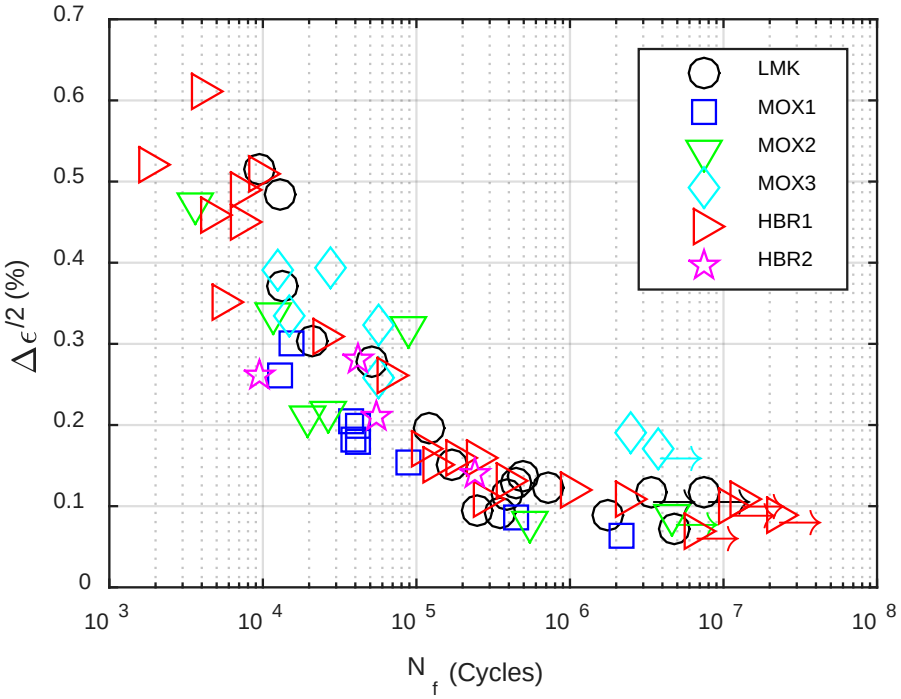

(e)

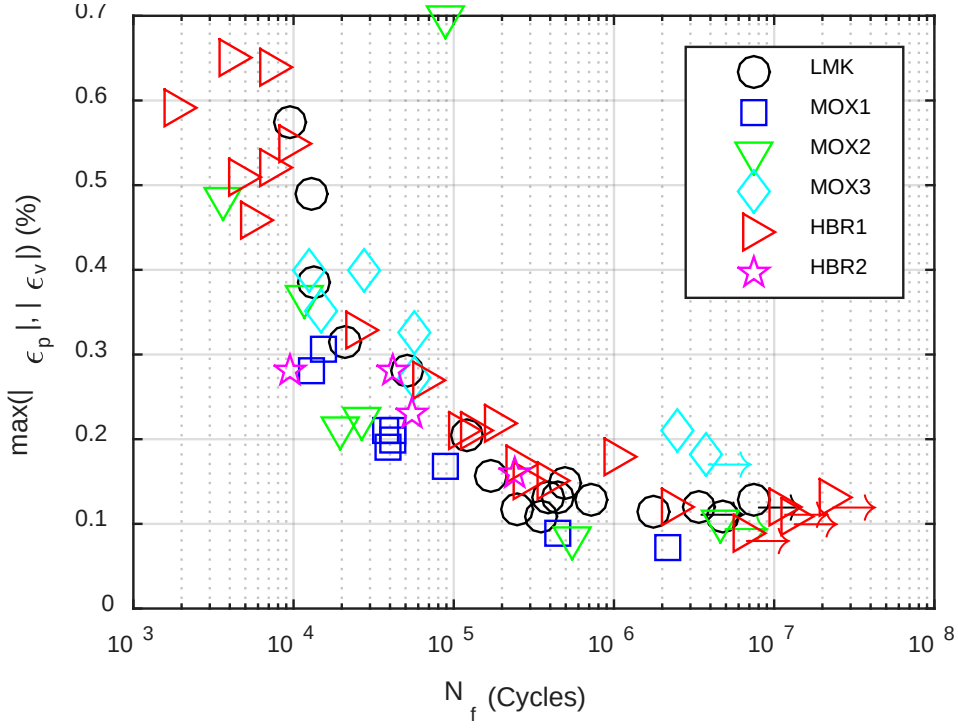

(f)

Fig. 17. (a) Moment amplitude, (b) stress amplitude, (c) curvature amplitude, (d) curvature maximum, (e) strain amplitude, and (f) strain maximum as a function of cycles or cycles to failure.

5.2 Remaining Issues with Curvature Measurement

5.2.1 Small Amplitude Curvature

In CIRFT tests, the small curvatures usually occur in the dynamic tests. Remaining issues exist with respect to the small curvature measurement.

1) *How close is the contact condition of SS-cladding-only surrogate rods to that of SNF rods?*
This question is critical because the contact dominates the sensor spacing used in the calculation of curvature. This is mainly because the cladding materials, and especially the surface condition of the SNF rods, vary from those of the surrogate rod. The initial engagement and the subsequent contact of LVDT probes with the rod will be affected by these factors.

2) *How much impact of the transverse motion of LVDT probes is imposed on curvature measurement?*
Clearance between the measurement probe and LVDT cylinder is designed to ensure a smooth longitudinal motion of the LVDT probe within the measurement cylinder. This clearance introduces an inevitable transverse motion of the probe, which affects the initial engagement of the probe with the rod and also the subsequent translational movement of the probe in the measurement.

3) *What is the effect of driving frequency on the curvature measurement?*
It has been shown that frequency has an effect on the response of bending rod. The issue remaining to be addressed here is to determine how the frequency will impact the curvature measurement itself. This effect occurs because the contact of probe against the rod is influenced by the dynamics of the system.

5.2.2 Large Amplitude Curvature

There are some outstanding issues with regards to the large curvature measurement.

1) *The impact of pellet-cladding mechanical interaction (PCMI) may be important when the deformation becomes large.*
This is obvious because the local plastic deformation can be substantial due to local buckling in compressive side, for instance. This alters the surface condition, and in turn, it alters the contact of the probe against the rod.

2) *How will the transverse motion of the probe be changed with large deformation?*
The transverse motion is associated with clearance of LVDT measurement. Large deformation of the rod may close the gap between the measurement rod and the cylinder on one side and open it on the other side.

3) *How is the correction applicable to the real SNF rods?*
The spacing correction relation has been developed using a flexible rod made of materials like polycarbonate. This provides a useful approach to investigate the response of the rod system in large deformation, but it needs to be justified before being migrated into the CIRFT data analysis.

6. CONCLUSION

1) The contact of the probe affects curvature measurement in current CIRFT tests. This effect can be corrected by sensor spacing, defined as the amount of separation between the three LVDT probes for curvature measurement.

2) The sensor spacing correction can be determined using a chisel-type probe. However, this method is limited in its application and cannot be implemented effectively.

3) The sensor spacing correction based on equivalent gage length has the required flexibility and can meet the challenges of this application.

4) The correction method based on the equivalent gage length has been demonstrated in this report in CIRFT data analysis for the dynamic tests on LMK (17), NA (6), and MOX (10) fuel rods.

5) Some important issues, such as the effects of large amplitude curvature, transverse movement of probes, etc., remain to be investigated.

6) The equivalent stress indeed collapsed the data points from all of the SNFs into a single zone. A detailed examination, based on the means trend curves of the corresponding subgroups, revealed that, at same stress level, fatigue lives display a descending order as follows: HBR, LMK, MOX. If looking at the strain, LMK fuel has a slightly longer fatigue life than HBR, but the difference is subtle.

7) The knee point in the curve of moment and curvature or equivalent quantities is more clearly defined for LMK and HBR fuels.

8) Both the 12 in. drop and RHT appears it could have a negative impact on the fatigue life of CIRFT specimens.

9) The effect of the thermal heating treatment on MOX fuel rod was relatively small at the higher amplitude but became significant at the low amplitude of moment. Thermal heating treatment tends to extend the fatigue life of specimens of MOX fuel rod. However, for HR4 CIRFT testing of the HBR rod, thermal heating treatment shows a negative impact on the fatigue life of the HBR rod. This may indicate that the effect of thermal heat treatment on SNF rods is likely to be material dependent.

REFERENCES

1. J.-A. J. Wang, H. Wang, Y. Yan, R. Howard, and B. Bevard, *High Burn-up Spent Fuel Vibration Integrity Study Progress Letter Report (Out-of-Cell Fatigue Testing Development–Task 2.1)*, ORNL/TM-2010/288, Oak Ridge National Laboratory, Oak Ridge, TN, January 2011.

2. J.-A. J. Wang, H. Wang, T. Tan, H. Jiang, T. Cox, and Y. Yan, *Progress Letter Report on U Frame Test Setup and Bending Fatigue Test for Vibration Integrity Study (Out-of-Cell Fatigue Testing Development–Task 2.2)*, ORNL/TM-2011/531, Oak Ridge National Laboratory, Oak Ridge, TN, January 2012.

3. J.-A. J. Wang, H. Wang, T. Cox, and Y. Yan, *Progress Letter Report on U-Frame Test Setup and Bending Fatigue Test for Vibration Integrity Study (Out-of-Cell Fatigue Testing Development–Task 2.3)*, ORNL/TM-2012/417, Oak Ridge National Laboratory, Oak Ridge, TN, August 2012.

4. J.-A. J. Wang, H. Wang, and Ting Tan, *An Innovative Dynamic Reversal Bending Fatigue Testing System for Evaluating Spent Nuclear Fuel Rod Vibration Integrity or Other Materials Fatigue Aging Performance*, ORNL Invention Disclosure 201102593, DOE S 124,149, April 8, 2011, patent in review, 13/396,413, February 14, 2012.

5. H. Wang, J.-A. J. Wang, T. Tan, H. Jiang, T. S. Cox, R. L. Howard, B. B. Bevard, and M. E. Flanagan, "Development of U-frame Bending System for Studying the Vibration Integrity of Spent Nuclear Fuel," *Journal of Nuclear Materials* 440, 201–213 (2013).

6. J.-A. J. Wang, H. Wang, B. B. Bevard, R. L. Howard, and M. E. Flanagan, "SNF Test System for Bending Stiffness and Vibration Integrity," *International High-Level Radioactive Waste Management Conference*, Albuquerque, NM, April 28–May 2, 2013.

7. J.-A. J. Wang, H. Wang, T. Cox, and C. Baldwin, *Progress Letter Report on Bending Fatigue Test System Development for Spent Nuclear Fuel Vibration Integrity Study (Out-of-Cell Fatigue Testing Development–Task 2.4)*, ORNL/TM-2013/225, Oak Ridge National Laboratory, Oak Ridge, TN (2013).

8. J.-A. J. Wang, H. Wang, B. B. Bevard, R. L. Howard, and M. E. Flanagan, "Reversible Bending Fatigue Test System for Investigating Vibration Integrity of Spent Nuclear Fuel During Transportation," *Proceedings of the 17th International Symposium on the Packaging and Transportation of Radioactive Materials,* PATRAM 2013, San Francisco, CA, August 18–23, 2013.

9. G. Bjorkman, "High Burnup Spent Fuel Testing Program Objectives," NRC Program Review Meeting, Oak Ridge National Laboratory, August 8, 2011.

[10] Jy-An Wang, Hong Wang, "CIRFT Testing Data Analyses and Updated Curvature Measurements," ORNL/SPR-2016/276, July 24, 2016

[11] Jy-An Wang, Hong Wang, Hao Jiang, Yong Yan, Bruce Bevard, "CIRFT Testing of High-Burnup Used Nuclear Fuel Rods from Pressurized Water Reactor and Boiling Water Reactor Environments," ORNL/SPR-2015/313, M2-FCRD-UFD-2015-000101, September 4, 2015

This page intentionally left blank